

Coupling deal.II and FROSch: A Sustainable and Accessible (O)RAS Preconditioner

A. Heinlein¹, S. Kinnewig^{2,3}, and T. Wick^{2,3}

¹TU Delft, DIAM, Faculty of EEMCS Numerical Analysis, Mekelweg 4, 2628 Delft, Netherlands

²Leibniz University Hannover, Institute of Applied Mathematics, Welfengarten 1, 30167 Hannover, Germany

³Cluster of Excellence PhoenixD (Photonics, Optics, and Engineering - Innovation Across Disciplines), Leibniz University Hannover, Germany

Abstract

In this work, restricted additive Schwarz (RAS) and optimized restricted additive Schwarz (ORAS) preconditioners from the Trilinos package FROSch (Fast and Robust Overlapping Schwarz) are employed to solve model problems implemented using deal.II (differential equations analysis library). Therefore, a Tpetra-based interface for coupling deal.II and FROSch is implemented. While RAS preconditioners have been available before, ORAS preconditioners have been newly added to FROSch. The deal.II-FROSch interface works for both Lagrange-based and Nédélec finite elements. Here, as model problems, nonstationary, nonlinear, variational-monolithic fluid-structure interaction and the indefinite time-harmonic Maxwell's equations are considered. Several numerical experiments in two and three spatial dimensions confirm the performance of the preconditioners as well as the FROSch-deal.II interface. In conclusion, the overall software interface is straightforward and easy to use while giving satisfactory solver performances for challenging PDE systems.

1 Introduction

Domain decomposition methods (DDMs) [71, 67, 73, 23] are a class of solvers, and preconditioners that allow for efficiently solving complex model problems arising from scientific and engineering applications. Their robustness enables the application to challenging problems that would otherwise require the use of direct solvers, which is infeasible for large problems due to the superlinear complexity of direct solvers. The restricted additive Schwarz (RAS) preconditioner [13] and optimized restricted additive Schwarz (ORAS) preconditioner [36] are popular choices of one-level Schwarz domain decomposition preconditioners. While RAS preconditioners are closely related to Lions' algorithm [62], as discussed in [27], ORAS preconditioners are a typical choice of preconditioners for wave problems due to a different choice of the transmission condition on the subdomain boundaries. However, both RAS and ORAS preconditioners are inherently unsymmetric, even if the original problem is symmetric, and therefore, cannot be employed with the conjugate gradient (CG) method; here, we consider the GMRES (generalized minimal residual) method [70] instead.

One-level DDMs, such as one-level RAS and ORAS preconditioners, are generally not scalable to large numbers of subdomains; the number of iterations will increase with the number of subdomains. To overcome this problem, a second level, which corresponds to solving a global coarse problem of a small dimension, can be introduced. If well chosen, the coarse problem enables the global transport of information required for numerical scalability, that is, scalability for increasing numbers of subdomains; however, since the coarse level introduces a global problem, it can also become a bottleneck for parallel scalability if its dimension is too large. If the coarse

problem can be solved efficiently (in parallel), two-level Schwarz preconditioners are a compelling choice for high-performance computing (HPC) applications. In order to avoid implementing RAS or ORAS preconditioners from scratch for various applications, it is desirable to have a sustainable, accessible implementation that can be adjusted to other application problems with minimal effort. To address this, we choose the FROSch [46, 47] domain decomposition solver framework, which is part of `Trilinos`, as the basis for implementing the preconditioners. Then, we couple it with the finite element library `deal.II` [3, 2]. `deal.II` is notable for its active community, comprehensive documentation, and numerous online tutorial examples.

The key contributions of this work are the implementation of the ORAS preconditioner in FROSch as well as the coupling of FROSch and `deal.II`. To this end, we construct and implement a software interface based on the newly developed `Tpetra-Interface of deal.II`. The performance is then demonstrated for two challenging model problems. First, nonstationary, nonlinear Fluid-Structure Interaction (FSI) is considered in both two and three spatial dimensions. A two-level RAS preconditioner with a specific coarse space from FROSch is employed here. Second, the new ORAS preconditioner, as well as the new FROSch-`deal.II` interface, are utilized to solve the time-harmonic Maxwell’s equations, again, both in two and three spatial dimensions. The main effort has been in the easiness of using the proposed software interface while giving satisfactory solver performances for challenging PDE problems, namely FSI and time-harmonic Maxwell’s equations. The code is available on GitHub¹, where we provide one example of the RAS preconditioner and one example of the ORAS preconditioner.

The outline of this paper is as follows. In Section 2, we provide a detailed introduction to Schwarz preconditioners, as well as a literature overview about Schwarz preconditioners. In Section 3, we describe the employed software packages, i.e., FROSch, `deal.II`, and the interface between these two. The partial differential equations considered as examples are introduced in Section 4. Finally, in Section 5, several numerical tests in two and three spatial dimensions for FSI and Maxwell’s equations substantiate our newly developed software interface.

2 Overlapping Schwarz Preconditioners

In this section, we introduce different versions of overlapping Schwarz preconditioners. Employing the Finite Element Method (FEM) to discretize (initial) boundary value problems on some computational domain Ω results at some point (after possible linearization) in sparse linear equation systems of the form

$$Ax = b. \tag{2.1}$$

For future reference, we use h to represent the mesh parameter, and the finite element space is denoted as $V := V^h(\Omega)$.

2.1 Additive Schwarz preconditioners

We decompose Ω into N non-overlapping subdomains $\Omega_1, \dots, \Omega_N$. In practice, this decomposition may, for instance, be obtained via a geometrical approach or via partitioning the dual graph of the triangulation using a graph partitioning tool, such as METIS [60], `Zoltan` [8], or `p4est` [12]. In the dual graph, the nodes of the graph are the finite elements, and two elements are connected via an edge if the finite elements have a common edge in the triangulation. Geometrical approaches, such as decomposing a rectangular domain into rectangular subdomains, are primarily limited to simple geometries and structured meshes, whereas graph partitioning approaches also apply to unstructured meshes.

Next, we extend these subdomains by k layers of elements, resulting in an overlapping domain decomposition with the subdomains $\Omega'_1, \dots, \Omega'_N$; see Figure 2.1. We denote the size of the overlap by $\delta = kh$ and define the local finite element spaces V_i on the local overlapping subdomains. Due to our construction, it follows that $V_i \subset V$, and we can define restriction

¹<https://github.com/kinnewig/dealii-FROSch-interface>

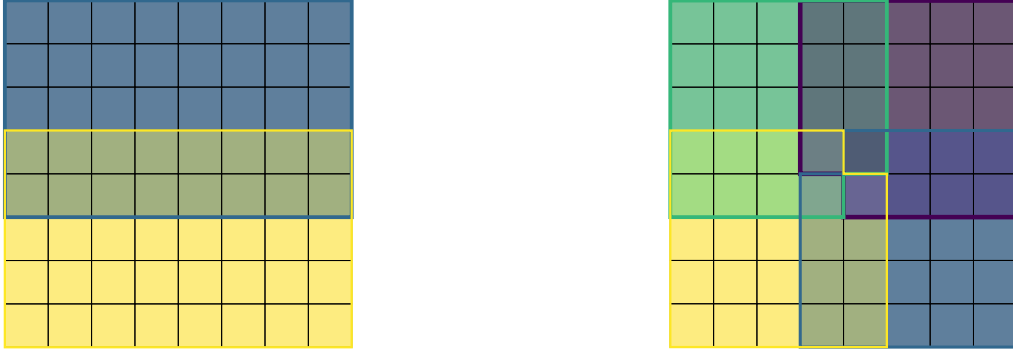


Figure 2.1: **Left:** A square domain divided into two subdomains, where the size of both subdomains was increased by one layer. **Right:** A square domain divided into four subdomains, where the size of all subdomains was increased by one layer. In both cases, the overlap was computed based on the dual graph.

operators $R_i : V \rightarrow V_i$ and corresponding prolongation operators $P_i : V_i \rightarrow V$, for all $1 \leq i \leq N$. Both can be represented as sparse binary matrices, and $P_i = R_i^\top$ is the transposed operator of R_i . Then, the additive overlapping Schwarz (AS) preconditioner is formally written as

$$M_{AS}^{-1} = \sum_{i=1}^N P_i A_i^{-1} R_i. \quad (2.2)$$

In the case of local exact solvers, we define the local subdomain matrices as

$$A_i = R_i A P_i, \quad \forall 1 \leq i \leq N. \quad (2.3)$$

Therefore, we choose $V_i = V_0^h(\Omega'_i)$, that is, the local finite element spaces are the restrictions of the global finite element space V to the local subdomains and with homogeneous Dirichlet boundary conditions on $\partial\Omega'_i$. Then, A_i can be obtained from A by extracting the submatrix corresponding to the interior finite element nodes of Ω'_i . This also directly implies that the A_i are invertible. For more details, we refer to the standard domain decomposition literature [71, 67, 73, 23].

For a Laplacian model problem, the matrix A is symmetric positive definite, and we can solve Equation (2.1) using the preconditioned conjugate gradient (PCG) method with the preconditioner given in Equation (2.2); we notice that M_{AS}^{-1} is then also symmetric positive definite. The convergence of PCG can then be bounded in terms of κ , namely the condition number of the preconditioned system matrix $M_{AS}^{-1}A$, i.e.,

$$\kappa(M_{AS}^{-1}A) \leq C \left(1 + \frac{1}{H\delta} \right). \quad (2.4)$$

Here, H is the subdomain diameter, and C is a constant that is independent of geometric constants H , h , and δ ; see, for instance [71, 67].

Remark 1 *The aforementioned approaches for the construction of overlapping domain decomposition cannot be performed in a fully algebraic way. We refer to fully algebraic as a method that requires only the fully assembled system matrix A . In particular, the geometry and/or the triangulation are required. The graph partitioning-based approach can also be carried out based on the sparsity pattern of A , that is, based on the node graph of the triangulation. Then, the overlap can be obtained by adding k layers of adjacent finite element nodes, where adjacency is defined based on the node graph. The resulting overlapping domain decomposition method then slightly differs, but the preconditioner becomes fully algebraic.*

2.2 Restricted additive Schwarz preconditioners

In [13], Cai and Sarkis introduced a restricted additive Schwarz (RAS) preconditioner, which often converges faster than the standard AS preconditioner and has a reduced communication cost in a distributed memory parallelization. However, the preconditioner is non-symmetric and, therefore, requires a different iterative solver than PCG, such as the generalized minimal residual (GMRES) method [70]. It is obtained by keeping A_i and R_i in Equation (2.2) while replacing the prolongation operators P_i by \hat{P}_i :

$$M_{\text{RAS}}^{-1} = \sum_{i=1}^N \hat{P}_i A_i^{-1} R_i. \quad (2.5)$$

Here, we define \hat{P}_i in such a way that

$$\sum_{i=1}^N \hat{P}_i R_i = I. \quad (2.6)$$

In the classical RAS preconditioner, this is achieved by partitioning the finite element nodes of the overlapping subdomains $\Omega'_1, \dots, \Omega'_N$ in a unique way. As discussed by Efstathiou and Gander in [27], this preconditioner relates to Lions' classical Schwarz method [62]. Equation (2.6) can alternatively be written using diagonal scaling matrices D_i :

$$\sum_{i=1}^N P_i D_i R_i = I. \quad (2.7)$$

The previous choice of \hat{P}_i corresponds to using binary scaling matrices D_i . However, we can also choose D_i to scale each finite element node by its inverse multiplicity with respect to the overlapping domain decomposition into $\Omega'_1, \dots, \Omega'_N$. Then, we obtain the following alternative formulation of the RAS preconditioner

$$M_{\text{RAS}}^{-1} = \sum_{i=1}^N P_i D_i A_i^{-1} R_i. \quad (2.8)$$

When using a non-binary scaling D_i , the preconditioner is sometimes called a scaled additive Schwarz (SAS) preconditioner.

2.3 Optimized Schwarz preconditioners

Finally, we introduce optimized additive Schwarz (OAS) and optimized restricted additive Schwarz (ORAS) preconditioners [72]. These are often employed for wave-type problems, such as Helmholtz equations or Maxwell's equations; cf. Section 4.2. Here, in particular, standard AS preconditioners often lead to suboptimal convergence rates compared to optimized Schwarz preconditioners. To this end, let us consider that Equation (2.1) results from the discretization of the Helmholtz equation

$$-\Delta u - \omega^2 u = f \quad \text{in } \Omega,$$

with some boundary conditions on $\partial\Omega$. Here, ω is the so-called wavenumber, and f is a source term.

In optimized Schwarz preconditioners, we replace the local problem matrices A_i in Equation (2.2) with the matrices B_i corresponding to local problems with different boundary conditions; recall that we automatically obtained homogeneous Dirichlet boundary conditions by the algebraic construction in Equation (2.3). In particular, the OAS preconditioner reads

$$M_{\text{OAS}}^{-1} = \sum_{i=1}^N P_i B_i^{-1} R_i, \quad (2.9)$$

and the ORAS preconditioner reads

$$M_{\text{ORAS}}^{-1} = \sum_{i=1}^N P_i D_i B_i^{-1} R_i. \quad (2.10)$$

In the most simple case, the matrix B_i is the discretization of the differential operator $-\Delta u - \omega^2 u$ using the local finite element space V_i and with Robin boundary operator $\left(\frac{\partial}{\partial n} + \alpha\right)$, $\alpha \in \mathbb{R}$, on the nodes of $\partial\Omega'_i \setminus \partial\Omega$. The Robin parameter α is a hyperparameter of the method, which can be tuned and gives the name to the optimized Schwarz method. In practice, the optimization can be done either theoretically [36] or computationally via numerical calibration. In a Krylov iteration, the application of B_i^{-1} typically corresponds to solving a system of the form

$$B_i y_i = R_i (b - Ax^{(k)}),$$

for y_i . The right-hand side is a restriction of the residual to Ω'_i , and $x^{(k)}$ is the iterate in the k th iteration. In particular, the restriction R_i is chosen such that $R_i (b - Ax^{(k)}) = 0$ for the nodes on $\partial\Omega'_i \setminus \partial\Omega$. As a result, we enforce the Robin boundary condition

$$\left(\frac{\partial}{\partial n} + \alpha\right) = 0 \quad (2.11)$$

on those nodes.

Other boundary conditions employing a perfectly matched layer (PML) [9] or other types of absorbing boundary conditions [37], are more complex and depend on more than one parameter but may yield even better convergence than Robin boundary conditions. In all optimized Schwarz methods, the matrix B_i cannot be obtained algebraically, as in Equation (2.3), due to the boundary conditions. Instead, the local system matrix has to be assembled separately to construct the preconditioner.

Remark 2 *In this paper, we focus on different variants of one-level Schwarz preconditioners. As indicated by the condition number bound in Equation (2.4), these are not scalable to large numbers of subdomains. When increasing the number of subdomains while keeping the computational domain Ω fixed, H is reduced, and hence, the condition number increases; cf. Equation (2.4). Even though the convergence of the non-symmetric one-level RAS and ORAS preconditioners cannot be bounded directly via the condition number, they encounter the same scalability issues.*

3 Coupling deal.II and FROSch

This section discusses the interface between `deal.II` and `FROSch`, which is based on the newly developed `Tpetra`-based `deal.II` interface to `Trilinos`.

3.1 FROSch domain decomposition preconditioner package: Background

`FROSch` (Fast and Robust Overlapping Schwarz) [46, 47] is a parallel domain decomposition preconditioning package, which is part of the `Trilinos` software library [54]. `FROSch` is based on the Schwarz framework [73] and allows for the construction of Schwarz operators by combining elementary Schwarz operators. A Schwarz operator is of the form of a preconditioner; for instance, the Schwarz operator corresponding to the AS preconditioner in Equation (2.2) reads

$$Q_{\text{AS}} = M_{\text{AS}}^{-1} A. \quad (3.1)$$

Multiple Schwarz operators Q_1, \dots, Q_M can be combined, for instance, in an additive way,

$$Q_{\text{ad}} = \sum_{i=1}^M Q_i,$$

or multiplicative way,

$$Q_{\text{mult}} = I - \prod_{i=1}^M (I - Q_i),$$

where I denotes the identity matrix; cf. [73]. In this sense, Q_{AS} can also be written as the sum of Schwarz operators $Q_i = P_i A_i^{-1} R_i$ as follows:

$$Q_{\text{AS}} = \sum_{i=1}^N Q_i.$$

We notice that M is some generic natural number, while N is the number of subdomains as before.

Remark 3 *We notice that Schwarz operators are often denoted by the symbol P_\star instead of Q_\star ; see, for instance, [73]. However, we decided on this notation since we already denote the prolongation operators in Section 2 as P_i .*

Another important algorithmic component of `FROSch` are extension-based coarse spaces, which allow for the construction of preconditioners using only algebraic information or only little geometric information. As discussed in Section 2.1 and Remark 1, the first level of Schwarz preconditioners can be constructed algebraically using only the fully assembled system matrix. For more details on the algebraic construction of `FROSch` preconditioners, see [47, 42, 44].

The main idea of the extension-based coarse spaces is that they do not require an explicit coarse triangulation. Still, the coarse spaces are constructed from non-overlapping domain decomposition. In particular, they employ ideas similar to non-overlapping domain decomposition methods, such as finite element tearing and interconnecting - dual primal (FETI-DP) [31, 30] and balancing domain decomposition by constraints (BDDC) [14, 18]. In particular, the coarse spaces in `FROSch` are based on generalized Dryja–Smith–Widlund (GDSW) [20, 19] coarse spaces. These have been extended to block systems [43], highly-heterogeneous problems [45], and composite Discontinuous Galerkin discretizations of multicompartment reaction-diffusion problems [58]. Moreover, reduced-dimension variants [21, 49] and multilevel extensions [52] have been developed to reduce the computational cost of solving the coarse problem. Using these techniques, `FROSch` preconditioners have been demonstrated to scale up to more than 220,000 cores on the Theta supercomputer; cf. [51]. In this work, we focus more on the one-level preconditioners and the first level of two-level preconditioners.

`FROSch` preconditioners are accessible via the unified solver interface `Stratimikos` of `Trilinos`. They can be constructed from a fully assembled, parallel distributed sparse matrix in both parallel linear algebra frameworks of `Trilinos`, `Epetra` or `Tpetra`; therefore, the lightweight interface class `Xpetra` is employed. By default, `FROSch` constructs the overlapping domain decomposition based on the (distributed-memory) parallel distribution of the input matrix using its sparsity pattern; cf. Remark 1. As a result, we obtain a one-to-one correspondence of MPI ranks and subdomains. Furthermore, `FROSch` preconditioners accept a parameter list as a second input, which can contain additional input parameters. The `Epetra` linear algebra package will soon be deprecated from `Trilinos`, so all packages will solely depend on `Tpetra`. Through `Tpetra`, `FROSch` is also able to make use of the performance portability model `Kokkos` [74] and the corresponding kernel library `KokkosKernels` [74, 68], allowing for node-level parallelization on CPUs and GPUs. The acceleration of `FROSch` preconditioners using GPUs has been demonstrated in [80]. Through the `Stratimikos` solver interface, `FROSch` preconditioners can easily be combined with iterative Kyrlov solvers from the `Belos` package [5]. Alternatively, `FROSch` preconditioners and `Belos` solvers can also be called and combined directly without using `Stratimikos`. For more details on the implementation in `FROSch`, we refer to [47, 42, 43, 46].

3.2 FROSch: Our new developments

Until now, FROSch has provided one- and two-level (R)AS preconditioners, focusing solely on an algebraic approach. Our aim is to extend FROSch also to provide an O(R)AS preconditioner. As previously discussed, assembling the local subdomain matrices B_i from Equation (2.10) requires geometric information.

Three new classes were added to FROSch for the implementation of the O(R)AS preconditioner. The *GeometricOverlappingOperator* is derived from the *OverlappingOperator* and acts as the basic building block for either the *GeometricOneLevelPreconditioner* or the *GeometricTwoLevelPreconditioner*. The basic design is similar to the *AlgebraicOverlappingOperator*, but instead of a completely algebraic approach, the *GeometricOverlappingOperator* provides the tools to compute the overlapping domains geometrically, where the overlap is computed based on the dual graph. The *GeometricOneLevelPreconditioner* and *GeometricTwoLevelPreconditioner* act similarly to the existing *OneLevelPreconditioner* and *TwoLevelPreconditioner* but are mandatory to expose the tools to compute the overlapping domains to the user. A detailed description of the functions in these three new classes is available as a doxygen documentation².

To construct the ORAS preconditioner, we begin with a parallel distributed triangulation, which is described by lists of vertices, cells, and auxiliary information. Here, each cell is described by $2 \cdot \text{dim}$ vertices. The auxiliary list has the same length as the cell list and contains additional information, such as material constants. This information must be provided by the finite element program in use. Each rank only stores all vertices, cells, and auxiliary data relevant to itself. Also, the dual graph of how the elements are connected to each other has to be provided from the finite element program. The parallel distributed triangulation is assumed to correspond to a non-overlapping domain decomposition. Based on the dual graph, FROSch generates the three lists of vertices, cells, and auxiliary information. These belong to the overlapping domain decomposition and are returned to the finite element program. Subsequently, local triangulations are created, each corresponding to one subdomain based on the overlapping vertex, cell, and auxiliary data. The local subsystem matrices B_i are assembled with the desired interface conditions on each subdomain. FROSch then constructs the O(R)AS preconditioner based on the subsystem matrices B_i ; cf. Equations (2.9) and (2.10).

To summarize, the overlapping domain decomposition is computed automatically based on the user-provided triangulation. However, the user must create local triangulations based on the three lists of vertices, cells, and auxiliary information and, based on that, the local mass matrix and local Neumann matrices with the interface conditions. We provide an example of how this can be done in `deal.II`. The preconditioner is automatically computed by FROSch based on the local system and interface matrices. Optionally, the interface conditions could be replaced with different absorbing interface conditions such as PML.

3.3 deal.II

`deal.II` (differential equations analysis library) [2, 3] is an open-source and widely adopted C++ library specifically designed for solving Partial Differential Equations (PDEs). Its versatility has led to its extensive use in academic research and commercial projects. Own examples from ourselves include phase-field fracture propagation in porous media in which up to five PDEs and variational inequalities couple using physics-based discretizations and physics-based solvers [75], with the open-source `pfm-cracks` module [53], as well as nonstationary fluid-structure interaction optimal control [78], with the open-source optimization toolkit `DOP-ELIB` [39] based on `deal.II`. In fact, repeated computations, such as in optimal control or parameter estimation, are a key reason why the performance of solvers is needed. We also refer to the `deal.II` tutorial page³ in which numerous further applications are described. One of the key attributes of `deal.II` is its high accessibility. This is largely attributed to its comprehensive documentation, active

²<https://github.com/kinnewig/Trilinos/tree/OptimizedSchwarz>

³<https://www.dealii.org/current/doxygen/deal.II/Tutorial.html>

community, and an extensive list of the previously mentioned tutorial steps. These tutorials offer detailed, step-by-step explanations for solving a wide array of equations and problems. The ten main features of `deal.II` are conveniently provided on the main webpage⁴.

The construction of one-level O(R)AS preconditioners requires knowledge of which matrix entries belong to the degrees of freedom (dofs) at the interface and, thus, cannot be performed algebraically as that information requires knowledge of the grid and how the dofs are distributed on the grid. For the two-level O(R)AS preconditioner, we may construct the second level algebraically, as in [47, 42, 44]. But since mesh information is readily available in the `deal.II-FROSch` interface and required for the construction of the first level, we also provide the index sets of the interface degrees of freedom to `FROSch` as an input. This is because the quality of the algebraic interface reconstruction may depend on the mesh structure and finite elements employed; cf. [44]. Providing the interface to `FROSch` as input ensures that the exact interface can be employed in the construction of the preconditioners.

4 Applications

In this section, we introduce two challenging applications in order to study the performance of our algorithms and the newly proposed software implementations.

4.1 Fluid-Structure Interaction

Fluid-structure interaction (FSI) [69, 6, 35] is one of the most challenging PDE systems for the following reasons. It involves the coupling of two physics, namely fluid flow and a solid. Large deformations are assumed, which require the modeling of both problems in their natural coordinate systems: fluid flow is modeled in Eulerian coordinates, and solids are modeled with Lagrangian coordinates. Moreover, the dynamics occur on a common interface, which needs to be resolved in the numerical approximation with sufficient accuracy to prescribe the dynamics to the respective other problem correctly. In order to couple both systems, different methods exist, one of which is the so-called arbitrary Lagrangian-Eulerian (ALE) approach ([24, 57, 25, 33]) in which fluid flow is re-written in general coordinates such that on the interface (and in the solid), Lagrangian coordinates are utilized while going away; we smoothly transition to Eulerian coordinates. To this end, we utilize $\widehat{\Omega}$ as the reference configuration where the computations occur. To obtain the physics, the ALE transformation $\widehat{\mathcal{A}}$ must be applied to obtain the physical FSI solution in Ω . This is also important when the FSI solution is displayed via a visualization program.

In FSI, three solution variables are coupled: vector-valued velocities v , scalar-valued pressure p , and vector-valued displacements u . The resulting discrete nonlinear equation systems must first be addressed with some nonlinear solver (often Newton's method), then handled internally with a linear solver. The linear systems have a saddle-point structure. The solution remains costly despite several solver developments, e.g., [41, 38, 15, 16, 34, 59, 17, 47, 48, 4, 79]. Specifically, the efficient solution for the three-dimensional case remains a challenge. For this reason, FSI has been chosen as one application for our `deal.II-FROSch` framework.

We denote by $\Omega := \Omega(t) \subset \mathbb{R}^d$, the domain of the FSI problem. The domain consists of two time-dependent subdomains $\Omega_f(t)$ and $\Omega_s(t)$. The FSI-interface between $\Omega_f(t)$ and $\Omega_s(t)$ is denoted by $\Gamma_I(t) = \partial\Omega_f(t) \cap \partial\Omega_s(t)$. The initial (or later reference) domains are denoted by $\widehat{\Omega}$, $\widehat{\Omega}_f$, and $\widehat{\Omega}_s$, respectively, with the interface $\widehat{\Gamma}_i = \partial\widehat{\Omega}_f \cap \partial\widehat{\Omega}_s$. Furthermore, we denote the outer boundary by $\partial\widehat{\Omega} = \widehat{\Gamma} = \widehat{\Gamma}_{\text{in}} \cup \widehat{\Gamma}_D \cup \widehat{\Gamma}_{\text{out}}$. Function values in Eulerian and Lagrangian coordinates are identified by

$$u_f(x, t) =: \widehat{u}_f(\widehat{x}, t), \quad \text{with } x = \widehat{\mathcal{A}}(\widehat{x}, t).$$

The ALE map is defined by

$$\widehat{\mathcal{A}}(\widehat{x}, t) := x = \widehat{x} + \widehat{u}(x, t)$$

⁴<https://www.dealii.org/about.html>

and typically obtained by solving an additional PDE. In this work, this is a nonlinear harmonic model, i.e., given \hat{u}_s , at each t_m for $m = 1, \dots, M$, find $\hat{u}_f: \hat{\Omega}_f \rightarrow \mathbb{R}^d$ such that

$$-\hat{\nabla} \cdot (\hat{\sigma}_{mesh}) = 0, \quad \hat{u}_f = \hat{u}_s \text{ on } \hat{\Gamma}_I, \quad \hat{u}_f = 0 \text{ on } \partial\hat{\Omega}_f \setminus \hat{\Gamma}_I, \quad (4.1)$$

with $\hat{\sigma}_{mesh} = \hat{\alpha}_u \hat{\nabla} \hat{u}_f$ and $\hat{\alpha}_u > 0$. The deformation gradient is given by

$$\hat{F} := \hat{\nabla} \hat{\mathcal{A}}(\hat{x}, t) = I_d + \hat{\nabla} \hat{u},$$

with I_d being the identity matrix, and its determinant is given by

$$\hat{J} := \det(\hat{F}).$$

The following problem statement is a composition of the incompressible Navier-Stokes equations, written in ALE coordinates, coupled to geometrically nonlinear elasticity. For more details on the derivation, we refer to [69], while our notation is based on [76, 77]. For the weak formulation, the function space is denoted by \hat{X} . Dirichlet boundary conditions are built into \hat{X} as usually done, while Neumann conditions arise through integration by parts in the weak form. Neumann conditions on the FSI-interface will cancel out as we have the equilibrium of normal stresses. For details, we refer to the previously mentioned references. Moreover, the specific boundary conditions, such as inflow, outflow, and no-slip conditions, are provided in each respective numerical test below. To this end, we have:

Problem 1 (Variational-monolithic space-time ALE FSI in $\hat{\Omega}$) *Let non-homogeneous Dirichlet inflow data, the remaining boundary conditions, and some initial data be given. Find a global vector-valued velocity, vector-valued displacements, and a scalar-valued fluid pressure, i.e., $\hat{U} := (\hat{v}, \hat{u}, \hat{p}) \in \hat{X}$ such that:*

Balance of fluid/solid momentum:

$$\begin{aligned} & \int_I \left(\left(\hat{J} \hat{\rho}_f \partial_t \hat{v}, \hat{\psi}^v \right)_{\hat{\Omega}_f} + \left(\hat{\rho}_f \hat{J} (\hat{F}^{-1} (\hat{v} - \hat{w}_A) \cdot \hat{\nabla}) \hat{v}, \hat{\psi}^v \right)_{\hat{\Omega}_f} + \left(\hat{J} \hat{\sigma}_f \hat{F}^{-T}, \hat{\nabla} \hat{\psi}^v \right)_{\hat{\Omega}_f} \right. \\ & \quad \left. - \left\langle \hat{\rho}_f \nu_f \hat{J} (\hat{F}^{-T} \hat{\nabla} \hat{v}^T \hat{n}_f) \hat{F}^{-T}, \hat{\psi}^v \right\rangle_{\hat{\Gamma}_{out}} + \left(\hat{\rho}_s \partial_t \hat{v}, \hat{\psi}^v \right)_{\hat{\Omega}_s} + \left(\hat{F} \hat{\Sigma}, \hat{\nabla} \hat{\psi}^v \right)_{\hat{\Omega}_s} \right) dt \\ & \quad + \left(\hat{J} \hat{\rho}_f (\hat{v}(0) - \hat{v}_0), \hat{\psi}^v(0) \right)_{\hat{\Omega}_f} + \hat{\rho}_s \left(\hat{v}(0) - \hat{v}_0, \hat{\psi}^v(0) \right)_{\hat{\Omega}_s} = 0 \end{aligned}$$

Mesh/solid 2nd equation:

$$\int_I \left(\left(\hat{\sigma}_{mesh}, \hat{\nabla} \hat{\psi}^u \right)_{\hat{\Omega}_f} + \hat{\rho}_s \left(\partial_t \hat{u} - \hat{v}, \hat{\psi}^u \right)_{\hat{\Omega}_s} \right) dt + \hat{\rho}_s \left(\hat{u}(0) - \hat{u}_0, \hat{\psi}^u(0) \right)_{\hat{\Omega}_s} = 0$$

Fluid mass conservation:

$$\int_I \left(\left(\hat{\nabla} \cdot (\hat{J} \hat{F}^{-1} \hat{v}), \hat{\psi}^p \right)_{\hat{\Omega}_f} \right) dt = 0 \quad (4.2)$$

for all $\hat{\Psi} = (\hat{\psi}^v, \hat{\psi}^u, \hat{\psi}^p) \in \hat{X}^0$. The fluid constitutive stress tensor is given by

$$\hat{\sigma}_f := -\hat{p}_f I_d + \hat{\rho}_f \nu_f (\hat{\nabla} \hat{v}_f \hat{F}^{-1} + \hat{F}^{-T} \hat{\nabla} \hat{v}_f^T),$$

modeling a Newtonian fluid. The viscosity and the density of the fluid are denoted by ν_f and $\hat{\rho}_f$, respectively. The solid constitutive stress tensors are given by the second Piola-Kirchhoff stress tensor

$$\hat{\Sigma} = \hat{\Sigma}_s(\hat{u}_s) = 2\mu \hat{E} + \lambda \text{tr}(\hat{E}) I_d, \quad (4.3)$$

where the Green-Lagrange strain tensor is given by

$$\hat{E} = \frac{1}{2} (\hat{F}^T \hat{F} - I_d).$$

Here, μ and λ are the Lamé coefficients for the solid. The solid density is denoted by $\hat{\rho}_s$. The resulting solid material model is of St. Venant Kirchhoff type.

The Rothe method (horizontal methods of lines) is employed for the discretization: first, discretizing in time, then in space. For temporal discretization, finite difference schemes are used, namely the (implicit) backward Euler scheme (BE), which is strongly A-stable but only first-order and dissipative. A second choice is the Crank-Nicolson scheme, which is A-stable, second-order, less dissipative, and well-suited for energy conservation problems. The time-discretized equations are the starting point for the Galerkin discretization in space. To this end, we construct finite dimensional subspaces $\hat{X}_h^0 \subset \hat{X}^0$ to find an approximate solution to the continuous problem. In the context of monolithic ALE formulations, the computations are done on the reference configuration $\hat{\Omega}$. We use two- or three-dimensional shape-regular meshes. A mesh consists of quadrilateral or hexahedral elements \hat{K} . They form a non-overlapping cover of the computation domain $\hat{\Omega} \subset \mathbb{R}^d$, $d = 2, 3$. The corresponding mesh is given by $\hat{\mathcal{T}}_h = \{\hat{K}\}$. The discretization parameter in the reference configuration is denoted by \hat{h} and is a cell-wise constant that is given by the diameter $\hat{h}_{\hat{K}}$ of the cell \hat{K} . The resulting nonlinear discrete systems are solved with a line-search-assisted Newton's method; see [76, 77]. The resulting linearized equation systems are solved using our new `deal.II-FROSch` software interface. Lastly, we mention that, in [77], our `deal.II` FSI code was published and later moved to Github⁵, serving as a starting point for our 2D FSI implementation. The 3D FSI code can be implemented accordingly, with its prior results shown in [76][Section 4.4].

4.2 Time-Harmonic Maxwell's Equations

Maxwell's equations [32, 65] are utilized in many modern research fields, from magnetic induction tomography (MIT) in healthcare [81], geo-electromagnetic modeling in geophysics [40], quantum computing [63] and optics/photonics [64].

Problem 2 (Time-Harmonic Maxwell's Equations) *Let us consider $\Omega \subset \mathbb{R}^3$, a bounded Lipschitz domain with a sufficiently smooth boundary $\Gamma = \Gamma^{inc} \cup \Gamma^\infty$. On Γ^∞ , an absorbing boundary condition is prescribed. One possible choice is the Robin boundary condition*

$$\mu^{-1} (\vec{n} \times (\text{curl}(\vec{u}))) - i\sqrt{\varepsilon}\omega (\vec{n} \times (\vec{u} \times \vec{n})) = 0, \quad (4.4)$$

which corresponds to the first-order approximation of the Sommerfeld radiation conditions. On Γ^{inc} , a boundary condition for a given incident electric field is prescribed.. The goal is to find the electric field $\vec{u} \in \mathbf{H}_{\text{curl}}(\Omega)$ such that, for all $\vec{\varphi} \in \mathbf{H}_{\text{curl}}(\Omega)$, the following equation holds:

$$\begin{aligned} \int_{\Omega} \left(\mu^{-1} \text{curl}(\vec{u}) \cdot \text{curl}(\vec{\varphi}) - \varepsilon\omega^2 \vec{u} \cdot \vec{\varphi} \right) dx + i\sqrt{\varepsilon}\omega \int_{\Gamma} (\vec{n} \times (\vec{u} \times \vec{n})) \cdot (\vec{n} \times (\vec{\varphi} \times \vec{n})) ds, \\ = \int_{\Gamma^{inc}} (\vec{n} \times (\vec{u}^{inc} \times \vec{n})) \cdot (\vec{n} \times (\vec{\varphi} \times \vec{n})) ds. \end{aligned} \quad (4.5)$$

Here, \vec{u}^{inc} with $\vec{n} \times \vec{u}^{inc} \in L^2(\Gamma^{inc}, \mathbb{C}^d)$ is a given incident electric field, $\mu \in \mathbb{R}^+$ is the relative magnetic permeability, $\varepsilon \in \mathbb{R}^+$ is the relative permittivity, $\omega = \frac{2\pi}{\lambda}$ is the wavenumber, and $\lambda \in \mathbb{R}^+$ is the wavelength. Finally, i is the imaginary number.

Remark 4 *System Equation (4.5) is called time-harmonic because the time dependence can be expressed by $e^{i\omega\tau}$, where $\tau > 0$ represents the time. We avoid the need for a time-stepping method, where possibly a high number of time steps are required until the harmonic state is reached. We refer the reader to [65] for a detailed derivation of the time-harmonic Maxwell's equations.*

Solving the indefinite time-harmonic Maxwell's equations is challenging, as the linear system resulting from a Finite Element (FE) discretization is ill-posed as the corresponding system matrix has positive and negative eigenvalues. One encounters similar difficulties in the numerical solution of the ill-posed Maxwell's equations, which also occur in the Helmholtz equation [29].

⁵<https://github.com/tomeswick/fsi>

Therefore, specialized techniques have to be employed. DDMs yield good performance compared with other techniques, especially when optimized interface conditions are used; cf. [22]. When dealing with Maxwell’s equations in the context of FE, it is necessary to use Nédélec elements to preserve the curl-conforming behavior of the underlying function spaces. As Nédélec elements are oriented, one has to take care of the orientations of each edge and face when creating the (overlapping) subdomains to match the original orientation. For a description of the orientation problem in the context of Nédélec elements, we refer the reader to [61]. All these technical details must be considered while constructing an O(R)AS preconditioner for Maxwell’s equations, making this a challenging application.

5 Numerical studies

In this section, we first demonstrate the performance and ease of use of the `deal.II-FROSch` interface by solving different FSI problems with the use of RAS. Secondly, we demonstrate the O(R)AS extension of the `deal.II-FROSch` interface on the example of time-harmonic Maxwell’s problems. To solve the linear problems on each subdomain, the direct solver MUMPS [1] was used. All results presented in this section were computed on a server with a $2 \times$ AMD EPYC 7H12 64-Core processor with 1024 GB of RAM.

5.1 Fluid-Structure Interaction

First, we consider a series of FSI problems using the two-level RAS preconditioner provided by FROSch in `deal.II`. Due to the equal-order discretization with $Q_1 \times Q_1 \times Q_1$ elements, we can employ a monolithic two-level Schwarz preconditioner similar to [50]. However, we use a two-level RAS preconditioner with a simple second level in which the coarse basis functions have constant nodal values within each partition of a unique partitioning of the finite element nodes; cf. [66]. This coarse space is algebraic, and it can be directly constructed using, for instance, the \hat{P}_i prolongation operators of the RAS preconditioner Equation (2.6), or the corresponding binary scaling matrices D_i ; cf. Equation (2.7). Even though this coarse space might not be optimal, we chose this two-level preconditioner as it still performed better than a one-level preconditioner, especially for a higher number of subdomains. For a brief comparison between the one-level and the two-level method, see the solver analysis in Section 5.1.1.

5.1.1 Example 1: 2D FSI-1 benchmark

This benchmark was proposed in [56], and results from various groups are shown in [11]. The characteristic feature of this benchmark is a steady-state solution, which we will approximate via a backward Euler time-stepping scheme.

Configuration, boundary conditions, quantities of interest The computational domain is defined by a rectangle with dimensions $L = 2.50$ m and $H = 0.41$ m; see Figure 5.1. Within this domain, there is an obstacle that is slightly offset from the center, represented by the circle with the center $C = (0.20$ m, 0.20 m) and the radius $r = 0.05$ m. On the circle, an elastic beam of length $l = 0.35$ m and height $h = 0.02$ m is attached, and the lower right end of that beam is located $A = (0.60$ m, 0.19 m). As material parameters, we consider a fluid density of $\rho_f = 1.00 \cdot 10^3$ kg/m³ the viscosity $\nu_f = 1.00 \cdot 10^{-3}$ m²/s. We consider a density of $\rho_s = 1.00 \cdot 10^3$ kg/m³ for the solid and a Lamé coefficient of $\mu = 0.50 \cdot 10^6$ kg/m s². For the boundary conditions on Γ_{inflow} , we consider $v_{\text{inflow}} = 0.20$ m/s to be the inflow velocity. On the outflow boundary, we have the do-nothing condition [55], namely, normal stresses equal to zero, which results in the correction term $\langle \hat{\rho}_f \nu_f \hat{J}(\hat{F}^{-T} \hat{\nabla} \hat{v}^T \hat{n}_f) \hat{F}^{-T}, \hat{\psi}^v \rangle_{\hat{\Gamma}_{\text{out}}}$ due to the symmetric stress tensor. Lastly, we prescribe no-slip conditions (homogeneous Dirichlet) on the top and bottom walls of the channel, i.e., $v = 0$. We use $\Delta t = 1.00$ s for the time step size.

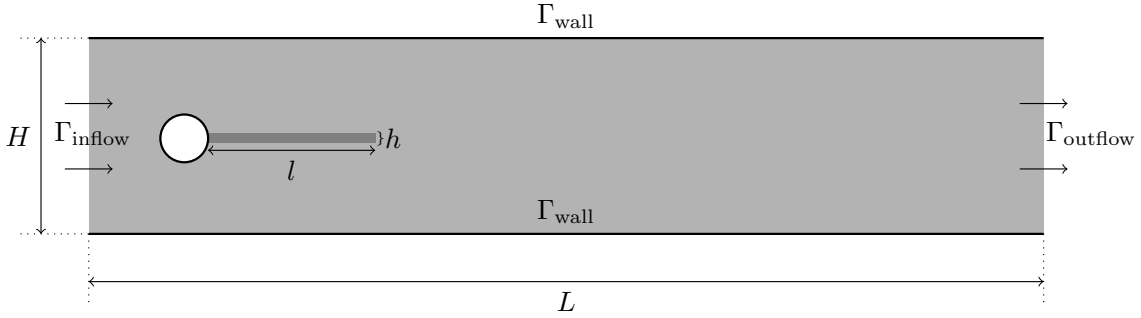


Figure 5.1: Flow around an obstacle to which an elastic beam is attached. In the two-dimensional case, the domain is a rectangle, and the obstacle is modeled as a cycle with the center $C(0.20, 0.20)$, and the lower right corner of the elastic beam is point $A(0.60, 0.19)$. In the three-dimensional case, the domain is a rectangular cuboid with depth D . The obstacle is modeled as a cylinder with the center C , and the front lower right corner of the elastic beam is point A .

Physics results To verify our results, we consider four quantities of interest [56], namely, the position $A := A(0.60, 0.19)$; see Figure 5.1. This is the lower right edge of the elastic beam, where we plot the x and y components individually. Moreover, we consider the values for the Face lift and the Face drag. These are evaluated around the cylinder and the elastic beam. For the mathematical formulae, we refer to [56, 77]. The results are visualized in Figure 5.2.

Solver analysis To evaluate the performance of the two-level RAS preconditioner, we examine the number of GMRES iterations necessary to solve the problem when we modify the number of subdomains and keep the number of dofs per subdomain constant. In two dimensions, this is achieved by a single global refinement and a fourfold increase in the number of subdomains. As we use a partition of unity with one function per subdomain for the coarse space, the coarse space size is given by $(2 \cdot \dim + 1)(ranks)$ because one constant value is assumed for each variable on any subdomain.

It is worth noting that the grid is first partitioned by `p4est` and then refined. Secondly, we consider the number of GMRES iterations dependent on the overlap between the subdomains. The results are shown in Table 5.1.

For the two-level method and for an overlap of $\delta/H = 20\%$ and 128 subdomains on average 468 GMRES iterations were required to solve the linear system, where a maximum of 589 GMRES iterations was encountered, and it took around 47.50 minutes. In comparison, the one-level method took an average of 555 iterations for the same case, where a maximum of 856 GMRES iterations was encountered, and it took around 56.78 minutes.

Ideally, with a two-level RAS preconditioner and a large number of subdomains, the number of GMRES iterations would remain constant. However, given our second level's simplicity, we observe an increase in the number of GMRES iterations, roughly proportional or slightly more, each time we quadruple the number of subdomains. This increase can be attributed to two factors. First, the default grid partitioning tool from `deal.II` is `p4est`[12], which was not designed with the application to domain decomposition in mind, leading to less-than-optimal partitioning (see Figure 5.3).

Second, the large time step size seems to contribute significantly to the high GMRES iteration counts; see also Table 5.2 for iteration counts for varying time step sizes as well as the results in Section 5.1.3. When the overlap is doubled, the number of GMRES iterations should be cut in half for large enough numbers of subdomains. Even though we observe a strong correlation between the overlap and the number of GMRES iterations, we do not observe this behavior. We suspect this might be related to the mesh partitioning obtained from `p4est`.

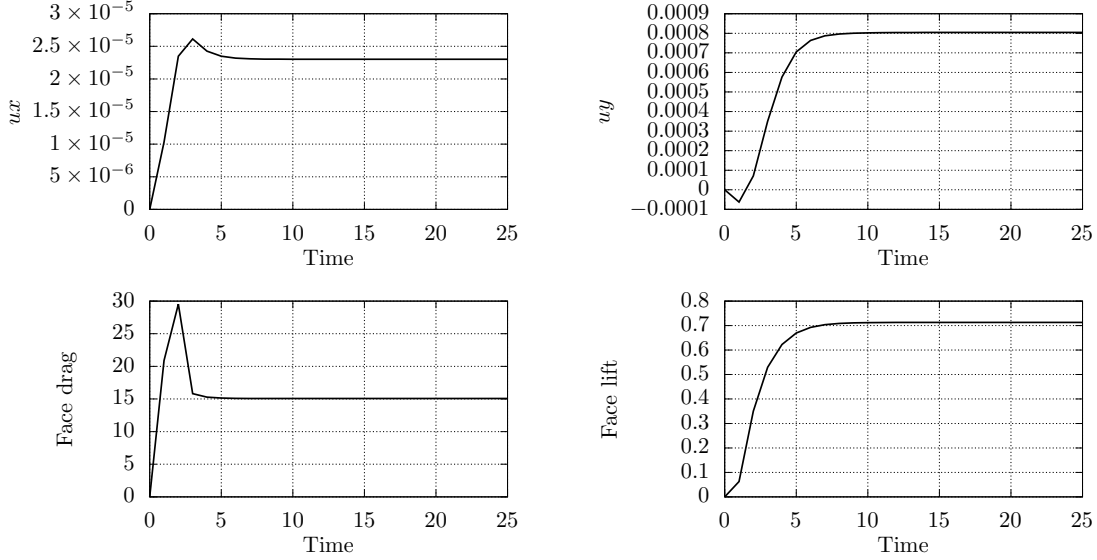


Figure 5.2: FSI-1 results. **Top left:** x -displacement in $A(0.6, 0.19)$. **Top right:** y -displacement in $A(0.6, 0.19)$. **Bottom left:** Face drag measured around the cylinder and the elastic beam. **Bottom right:** Face lift measured around the cylinder and the elastic beam.



Figure 5.3: The domain decomposition of the FSI-1 benchmark, as obtained by applying `p4est`. There are non-connected subdomains, as well as very long subdomains, which is less than optimal for a domain decomposition.

| ranks | dofs | Overlap | | $\delta/H = 10\%$ | $t_{10\%}^{\text{walltime}}$ | $\delta/H = 20\%$ | $t_{20\%}^{\text{walltime}}$ |
|-------|---------|------------------|-----------------------------|-------------------|------------------------------|-------------------|------------------------------|
| | | $\delta/H = 5\%$ | $t_{5\%}^{\text{walltime}}$ | | | | |
| 2 | 4 070 | 19.94 (25) | 1.0 min | 13.81 (16) | 1.0 min | 10.03 (12) | 1.1 min |
| 8 | 15 620 | 91.15 (107) | 1.6 min | 59.27 (74) | 1.7 min | 39.01 (50) | 2.4 min |
| 32 | 61 160 | 331.15 (549) | 3.9 min | 171.77 (202) | 3.7 min | 102.70 (118) | 5.4 min |
| 128 | 242 000 | > 1000 | — | > 1000 | — | 468.30 (589) | 47.5 min |

Table 5.1: Overview of the wall times and the average number of GMRES iteration steps required to solve the first 25 time steps of the FSI-1 problem in dependence on the number of used ranks, which corresponds to the number of subdomains and the overlap between the subdomains. The number in the brackets shows the highest number of GMRES iterations encountered. We consider the average of GMRES iterations here as a Newton method, and a time-step method is performed to solve the FSI problem.

| time step size | 1.0000 | 0.5000 | 0.2500 | 0.1250 | 0.0625 |
|------------------|--------|--------|--------|--------|--------|
| GMRES iterations | 346.63 | 255.16 | 221.62 | 199.60 | 178.99 |

Table 5.2: The number of GMRES iterations in dependency of the time step size, on the example of the FSI-1 benchmark with 61 160 dofs, $\delta/H = 5\%$ overlap and 128 subdomains.

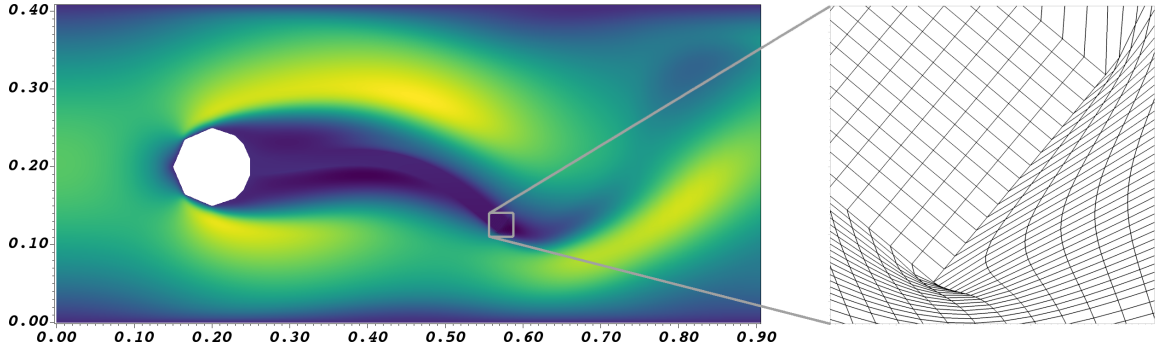


Figure 5.4: **Left:** Plot of the resulting velocity into x -direction from the flow around the cylinder at time step $t = 10$ s. **Right:** The mesh deformation at the tip of the elastic beam at time step $t = 10$ s.

5.1.2 Example 2: 2D FSI-2 benchmark

This benchmark was also proposed in [56], but yields periodic solutions and the von Karman vortex street. Numerous results for comparison were published in [56] and [76, 77].

Configuration, boundary conditions, quantities of interest We consider the same domain as for the FSI-1 example in Section 5.1.1; see Figure 5.1. As material parameters, we consider the same parameters for the fluid as in the FSI-1 example. For the solid, we consider a density of $\rho_s = 1.00 \cdot 10^4 \text{ kg/m}^3$ and a Lamé coefficient of $\mu = 0.50 \cdot 10^6 \text{ kg/m s}^2$. For the boundary conditions on Γ_{inflow} , we consider $v_{\text{inflow}} = 1.00 \text{ m/s}$ to be the inflow velocity. The other boundary conditions are the same as above. For the time step size we use $\Delta t = 1.00 \cdot 10^{-2} \text{ s}$.

Physics results In this example, a periodic state is obtained [56, 77]. The FSI-2 benchmark is the most difficult of all three proposed benchmarks as large deformations of the elastic beam occur, requiring a robust mesh motion model to avoid mesh distortion [76]; a graphical illustration of the highest deflection is given in Figure 5.4. To represent this periodic behavior, we again focus on the point $A(0.6, 0.19)$, that is, the lower left point of the beam. Our analysis focuses on the periodic state, and all findings are compared to [56, 77, 76]. Therefore, we only consider the time $t > 14 \text{ s}$ as proposed in [56]. In Figure 5.5, the periodic motion in terms of the y displacements can be observed. Our findings for drag and lift slightly differ from the literature values because we use equal-order finite elements and a simple pressure stabilization, which enters into the stress evaluation and thus slightly alters drag and lift values. Overall, the behavior of all four quantities of interest is in an acceptable range and confirms the correctness of the implemented FSI problem. Finally, the minimal \hat{J} is plotted as well, and the nominal minimal value is $8 \cdot 10^{-4}$, which shows that the chosen mesh motion model still works but is close to its limit.

Solver analysis As above, we study the correlation between the number of subdomains and GMRES iterations and the correlation between overlap and GMRES iterations. The results are shown in Table 5.3. Here, we consider the average values over the first 200 time steps. Here, the number of GMRES iterations increases less than for the FSI-1 example. Going from 32 to 128 subdomains, the number of GMRES iterations doubles, even though the number of subdomains quadruples. This is because of the smaller time step size. As shown in Table 5.2, there is a strong correlation between the time step size and the number of GMRES iterations.

The computation of 1500 time steps with 242 000 dofs took roughly 36.39 hours with 20% overlap. The average number of Newton steps per time step is 5. The minimal encountered number is 1, and the highest encountered number is 16 (where the mesh is close to degeneration with \hat{J} close to zero). As a result, on average, the solution and assembly of each linear system took around 16.67 seconds.

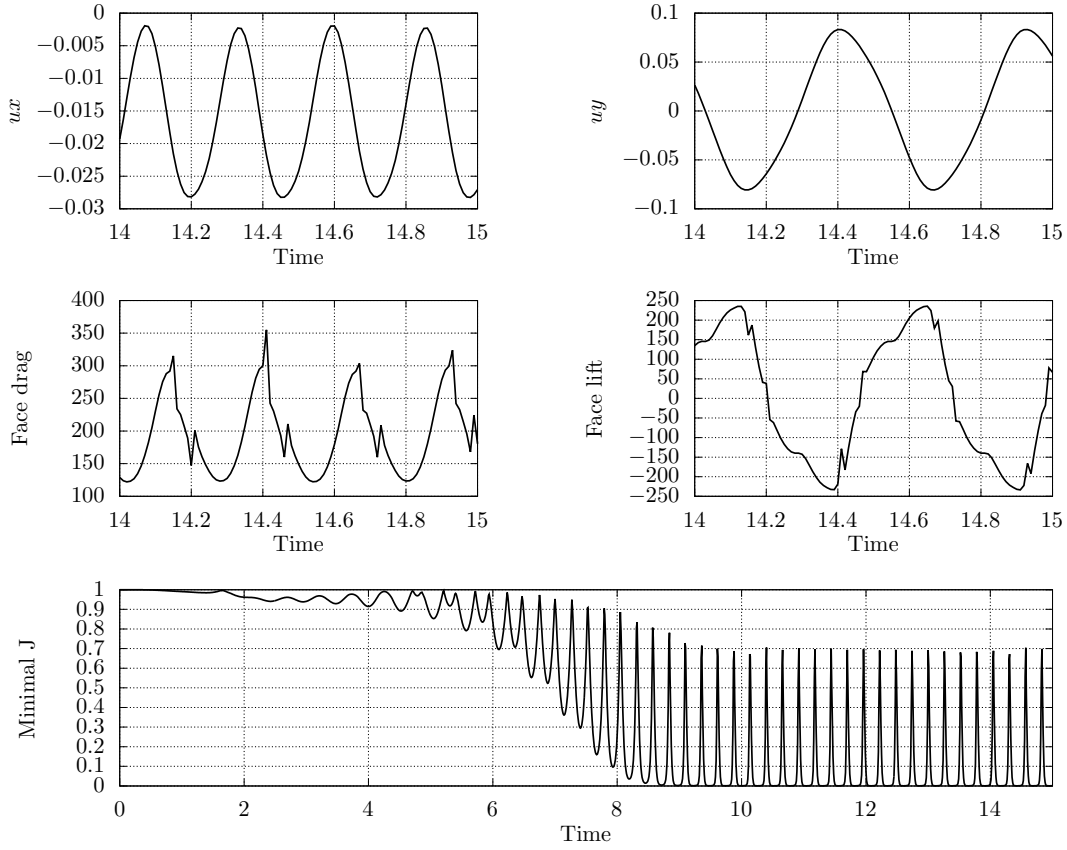


Figure 5.5: FSI-2 results. **Top left:** x -displacement in $A(0.6, 0.19)$. **Top right:** y -displacement in $A(0.6, 0.19)$. **Mid left:** Face drag. **Mid right:** Face lift. **Bottom:** Time evolution of the minimal \hat{J} (determinant of the deformation gradient \hat{F}) over all 1500 time steps.

| ranks | dofs | Overlap | | $\delta/H = 10\%$ | $t_{10\%}^{\text{walltime}}$ | $\delta/H = 20\%$ | $t_{20\%}^{\text{walltime}}$ |
|-------|---------|------------------|-----------------------------|-------------------|------------------------------|-------------------|------------------------------|
| | | $\delta/H = 5\%$ | $t_{5\%}^{\text{walltime}}$ | | | | |
| 2 | 4 070 | 19.99 (22) | 6.5 min | 13.9 (15) | 6.60 min | 11.0 (12) | 7.1 min |
| 8 | 15 620 | 68.32 (82) | 10.0 min | 47.6 (54) | 10.77 min | 33.7 (39) | 15.3 min |
| 32 | 61 160 | 129.98 (172) | 15.0 min | 88.1 (112) | 17.57 min | 63.1 (75) | 27.5 min |
| 128 | 242 000 | 240.42 (355) | 77.2 min | 163.4 (211) | 91.48 min | 117.1 (155) | 128.7 min |

Table 5.3: Overview of the wall times and the average number of GMRES iteration steps required to solve the first 200 time steps of the FSI-2 problem in dependence on the number of used ranks and the overlap between the subdomains. The number in the brackets shows the highest number of GMRES iterations encountered.

5.1.3 Example 3: 2D elastic lid-driven cavity

In this example, we consider a test case in which the solid covers a larger part of the overall domain [26]. We adapt the setting to have the solid cover a larger part of the domain.

Configuration, boundary conditions, quantities of interest For the computational domain, see Figure 5.6. Here, we consider the length $L_{\text{left}} = L_{\text{center}} = L_{\text{right}} = 0.50$ m and the height $H_{\text{solid}} = H_{\text{fluid}} = H_{\text{flow}} = 0.25$ m. As a material parameter, we consider the fluid to have the same parameters as in FSI-1; see Section 5.1.1. We consider a density structure of $\rho_s = 1.00$ kg/m³ for the solid. The Lamé coefficient is $\mu = 1.00 \cdot 10^2$ kg/m s². For the boundary conditions on Γ_{inflow} , we consider $v_{\text{inflow}} = 2.00$ m/s to be the inflow velocity. The other boundary conditions are the same as in the previous examples: do-nothing outflow and no slip on the walls. We use $\Delta t = 1.00$ s for the time step size.

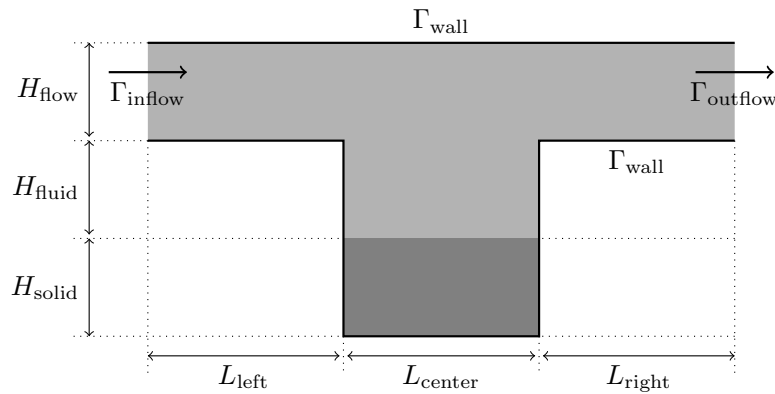


Figure 5.6: Configuration of the lid-driven cavity with the elastic bottom (dark gray) in the cavity.

Physics results In this case, a vortex forms in the cavity, deforming the elastic solid at the bottom of the solid. To verify our results, we consider the point $A = (0.75 \text{ m}, 0.25 \text{ m})$, which sits in the center of the interface between the solid and the liquid; see Figure 5.6. In Figure 5.7, the x and y components of the point A are plotted. Moreover, the normal stresses (named Face drag and Face lift) are shown. The results correspond to what we expected, as one can observe that the point A is shifted down by the vortex forming in the liquid above the solid.

| ranks | dofs | Overlap | | $\delta/H = 10\%$ | $t_{10\%}^{\text{walltime}}$ | $\delta/H = 20\%$ | $t_{20\%}^{\text{walltime}}$ |
|-------|---------|------------------|-----------------------------|-------------------|------------------------------|-------------------|------------------------------|
| | | $\delta/H = 5\%$ | $t_{5\%}^{\text{walltime}}$ | | | | |
| 2 | 6 885 | 31.17 (39) | 28.13 min | 17.31 (19) | 28.10 min | 15.03 (16) | 28.45 min |
| 8 | 26 565 | 103.71 (115) | 27.38 min | 42.74 (50) | 27.13 min | 30.74 (35) | 27.78 min |
| 32 | 104 325 | 223.13 (244) | 27.48 min | 101.56 (110) | 26.73 min | 71.18 (76) | 28.10 min |
| 128 | 413 445 | 472.00 (555) | 52.82 min | 252.76 (287) | 42.75 min | 170.85 (189) | 48.33 min |

Table 5.4: Overview of the wall times and the average number of GMRES iteration steps required to solve the first 50 time steps of the lid-driven-cavity problem in dependence on the number of used ranks and the overlap between the subdomains. The number in the brackets shows the highest number of GMRES iterations encountered.

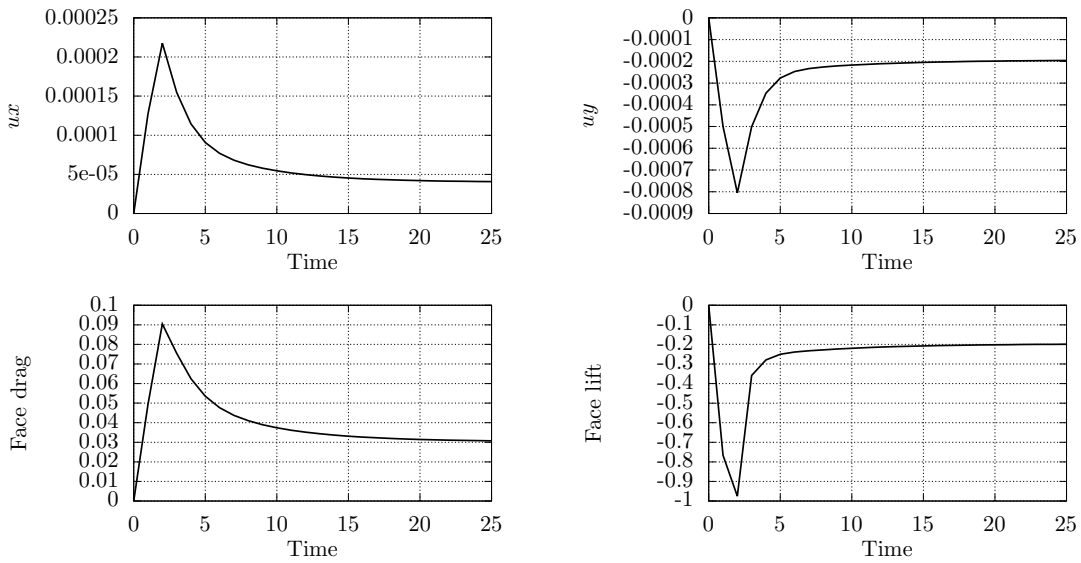


Figure 5.7: Results from the lid-driven cavity with elastic bottom. **Top left:** x -displacement in $A = (0.75, 0.25)$. **Top right:** y -displacement in $A = (0.75, 0.25)$. **Bottom left:** Face drag (normal stresses in x -direction on the interface). **Bottom right:** Face lift (normal stresses in y -direction on the interface).

Solver analysis In this example, a larger part of the domain is covered by the solid, which is beneficial for the RAS preconditioner. As we can see, when we compare the results in Table 5.4 to the above examples, the number of GMRES iterations grows less in dependency on the number of subdomains than it does in the FSI-1 example, even though a time step size of $\Delta t = 1.00$ s was used here as well.

In the computation with 20% overlap, the average number of Newton steps per time point t_n is 2. The minimal encountered number of Newton iterations is 1, and the highest encountered number is 4. As a result, on average, the solution and assembly of each linear system took around 33.72 seconds.

5.1.4 Example 4. 3D-FSI: 3D elastic bar behind a square cross-section

This 3D-FSI example is inspired by [76], which is an extension of the FSI-1 benchmark into three spatial dimensions. Specifically, a steady-state solution is obtained; see Figure 5.8. A cross-section of the computational domain is displayed in Figure 5.1.

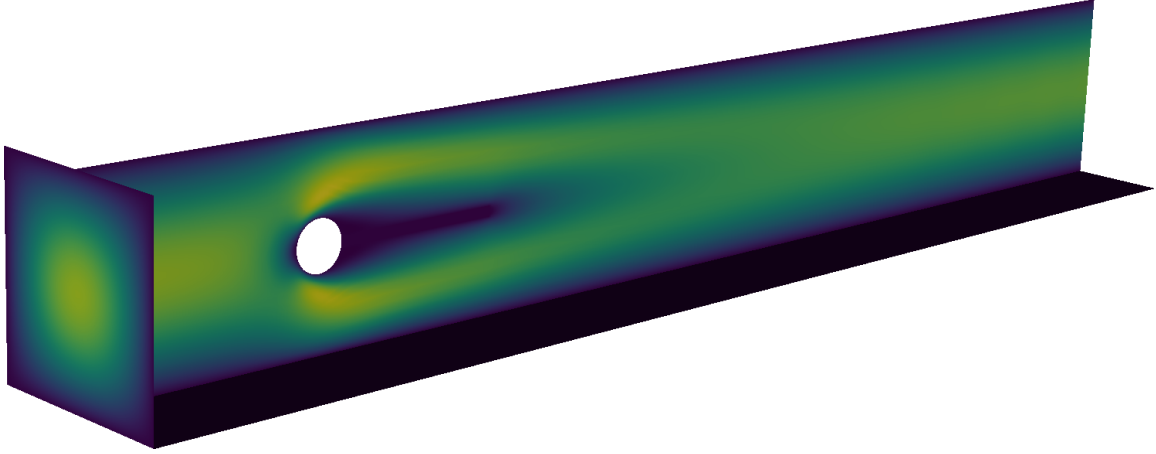


Figure 5.8: 3D-FSI example. The plot of the x -velocity at timestep $t = 25$ s displaying the final steady-state solution.

Configuration, boundary conditions, quantities of interest For the dimensions of the cuboid, the height is $H = 0.41$ m, the length $L = 2.80$ m, and the depth is $D = 0.41$ m. The center of the cylinder is $C = (0.50 \text{ m}, 0.20 \text{ m}, 0.00 \text{ m})$ with the radius $r = 0.05$ m. The front, lower right edge of the elastic beam is located at $A = (0.90 \text{ m}, 0.19 \text{ m}, 0.10 \text{ m})$. The other end is attached to the cylinder. The elastic beam has a length of $l = 0.45$ m, a height of $h = 0.02$ m, and a depth of $d = 0.20$ m. For the material parameters and boundary conditions, we assume the same as in the previous example FSI-1 in Section 5.1.1. We use $\Delta t = 1.00$ s for the time step size.

Physics results After some initialization time, the system assumes a steady state, as in the FSI-1 example. For the evaluation, we consider the x , y , and z components of point A, as well as the Face drag and the Face lift in Figure 5.9. In the time-dependent position of point A, the Face drag, and the Face lift, we can observe that the system converges against a steady state, as expected. The velocity in the x -direction inside the cuboid is shown in Figure 5.8.

Solver analysis We study the correlation between the number of subdomains and the number of GMRES iterations for the three-dimensional case, similar to the previous examples. To keep the number of dofs per subdomain constant, we globally refine once and multiply the number of subdomains by a factor of eight. As before, we also study the correlation between the number of GMRES iterations and the size of the overlap between subdomains. If we increase the number of subdomains by a factor of eight, the number of GMRES iterations grows by a factor of four or less. The number of GMRES iterations grows less in dependence on the number of subdomains compared to the example in Section 5.1.1, even though the main difference between these two examples is the spatial dimension. The results are shown in Table 5.5.

For 20% overlap, the average number of Newton steps per time point t_n is 6 iterations. The minimal encountered number of Newton iterations is 6, and the highest encountered number is 9 iterations. This implies that, on average, the solution and assembly of each linear system took around 4.41 minutes.

5.2 Time-Harmonic Maxwell's Equations

We consider Maxwell's equations as a second class of examples to demonstrate the performance of the one-level ORAS preconditioner. As discussed in [22], classical (R)AS preconditioners do not yield optimal performance in these kinds of problems. As the boundary condition for the local subdomain matrices B_i , we chose an easy-to-implement Robin-type interface condition shown in Equation (4.4) and the Robin parameter to be $\alpha = 1.0$. To ensure the correctness of the

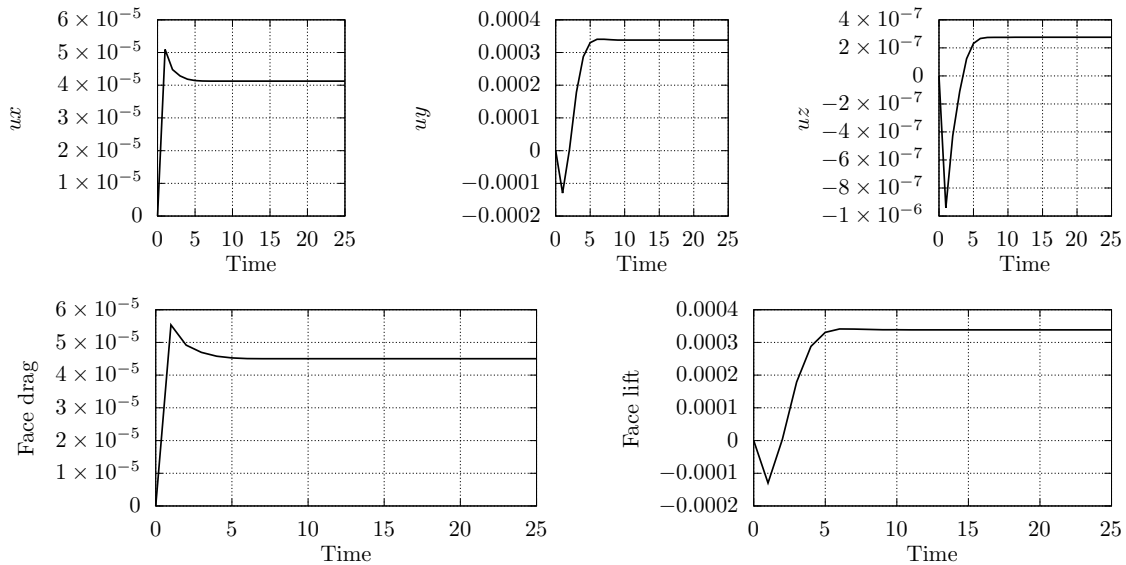


Figure 5.9: Results from the 3D-FSI problem. **Top left:** x -displacement of the point A of the elastic beam, i.e., the front lower right, a static state is assumed after some time. **Top center:** y -displacement of the point A of the elastic beam. **Top right:** z -displacement of the point A of the elastic beam. **Bottom left:** Global Face drag plotted against the time. **Bottom right:** Global Face lift plotted against the time.

| ranks | Overlap | | | | |
|-------|-----------|-------------------|------------------------------|-------------------|------------------------------|
| | dofs | $\delta/H = 10\%$ | $t_{10\%}^{\text{walltime}}$ | $\delta/H = 20\%$ | $t_{20\%}^{\text{walltime}}$ |
| 2 | 19 278 | 23.83 (26) | 17.4 min | 16.21 (20) | 17.4 min |
| 16 | 135 660 | 95.13 (104) | 59.5 min | 74.31 (83) | 103.8 min |
| 128 | 1 014 552 | 266.22 (291) | 424.7 min | 190.09 (209) | 687.7 min |

Table 5.5: Overview of the wall times and the average number of GMRES iteration steps required to solve the first 25 time steps of the 3D-FSI example in dependence on the number of used ranks and the overlap between the subdomains. The number in the brackets shows the highest number of GMRES iterations encountered. As we observed poor convergence for $\delta/H = 5\%$, we skip this case here.

results computed by our Maxwell solver, we conducted a comparative analysis with a reference Maxwell solver computing exactly the same problem statement. As reference solver, we use the Maxwell solver described in [7], which employs MUMPS; therefore, we could compute reference solutions for the 2D and 3D simple waveguide. In all cases, it holds for both numerical solutions $\|u_{\text{ref}} - u_{\text{ORAS}}\|_{L_\infty} < 10^{-12}$, where u_{ref} is the numerical solution computed by the reference Maxwell solver, and u_{ORAS} is the numerical solution of the Maxwell solver developed in this paper. It can be inferred that the physics are correct employing our new solver.

As for the third example, we consider a real-world application closely related to the problem discussed in [7]. In all experiments, we consider a wavelength of 632.8 nm, corresponding to the light emitted by a Helium-Neon laser. As a material with a higher refractive index, we are using quartz (SiO_2), which has, for the considered wavelength, a refractive index of $n_{\text{SiO}_2@632.8 \text{ nm}} = 1.4570$ ($\mu_{\text{SiO}_2} = 1.0000$ and $\varepsilon_{\text{SiO}_2} = n_{\text{SiO}_2}^2$). As a cladding material, we assume air with the refractive index $n_{\text{air}} = 1.0000$, ($\mu_{\text{air}} = 1.0000$, $\varepsilon_{\text{air}} = 1.0000$).

In this subsection, we consider a one-level preconditioner; therefore, we expect the number of GMRES iterations to increase with the number of subdomains. Even though Equation (2.4) cannot be applied directly to the case of using GMRES for Maxwell's equations, the condition number bound for the Laplace would indicate a condition number of $\kappa(M_{AS}^{-1}) \leq C(1 + 1/\beta H^2)$ for $\delta/H := \beta$ to be constant. Then, if we quadruple the number of subdomains in a two-dimensional setting with a structured domain decomposition, H is cut in half. Therefore, the condition number is multiplied by a factor of four, i.e., the number of GMRES iterations will increase as well.

Finally, we mention that we consider Nédélec elements of the lowest order, and our findings are compared to [7]. Here, we partition the grid using METIS [60].

5.2.1 Example 1: 2D Simple Waveguide

As a first example, we consider a simple model of a two-dimensional waveguide.

Configuration, boundary conditions, quantities of interest The waveguide is modeled by the domain $\Omega = (0, W) \times (0, L) = (0, 2) \times (0, 6) \mu\text{m}$, which includes a second rectangular subdomain of a material with a higher refractive index with width $R = 0.8 \mu\text{m}$ at its center. The geometry of the model is shown in Figure 5.10 (left). Moreover, $\Gamma_{\text{inc}} = (0, 2) \times \{0\} \mu\text{m}$ is the boundary with the incident boundary condition. All other boundaries, represented by Γ_∞ , are characterized by absorbing boundary conditions, for which we choose homogeneous Robin boundary conditions. The incident electric field is modeled by $u_{\text{inc}} = \exp(-100/\mu\text{m}^2(x^2)) \vec{e}_x$, where \vec{e}_x is the unit vector in the x -direction.

Physics results Figure 5.11 (left) shows the intensity distribution of the electric field forming inside the two-dimensional waveguide. As we only consider the intensity of the electric field here, we can see the formation of waves inside the waveguide, as one would expect.

Solver analysis Similar to the FSI problems, we are interested in the correlation of GMRES iterations with the overlap and the number of subdomains; the corresponding results are shown in Table 5.6. To keep the number of dofs per subdomain constant, we used one global refinement and increased the number of subdomains by a factor of four. The number of GMRES iterations grows at a similar rate as the number of subdomains, which is the expected behavior for a one-level method.

5.2.2 Example 2: 3D Simple Waveguide

This example is the three-dimensional variant of the example discussed above. We consider a simplified glass fiber model consisting of one material with a higher refractive index in the center surrounded by a material with a lower refractive index.

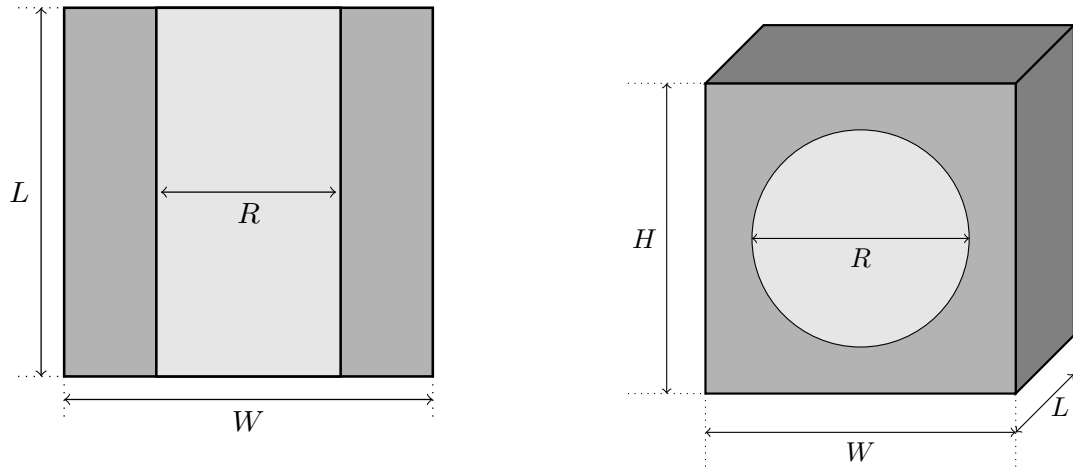


Figure 5.10: **Left:** Model of a simplified two-dimensional waveguide, the light gray area indicates the core, i.e., the domain with a higher refractive index, and the dark gray area indicates the cladding, i.e., the domain with a lower refractive index. **Right:** Model of a simplified glass fiber, i.e., a simple waveguide. Like the two-dimensional waveguide, the light gray domain indicates the core and the dark gray area indicates the cladding.

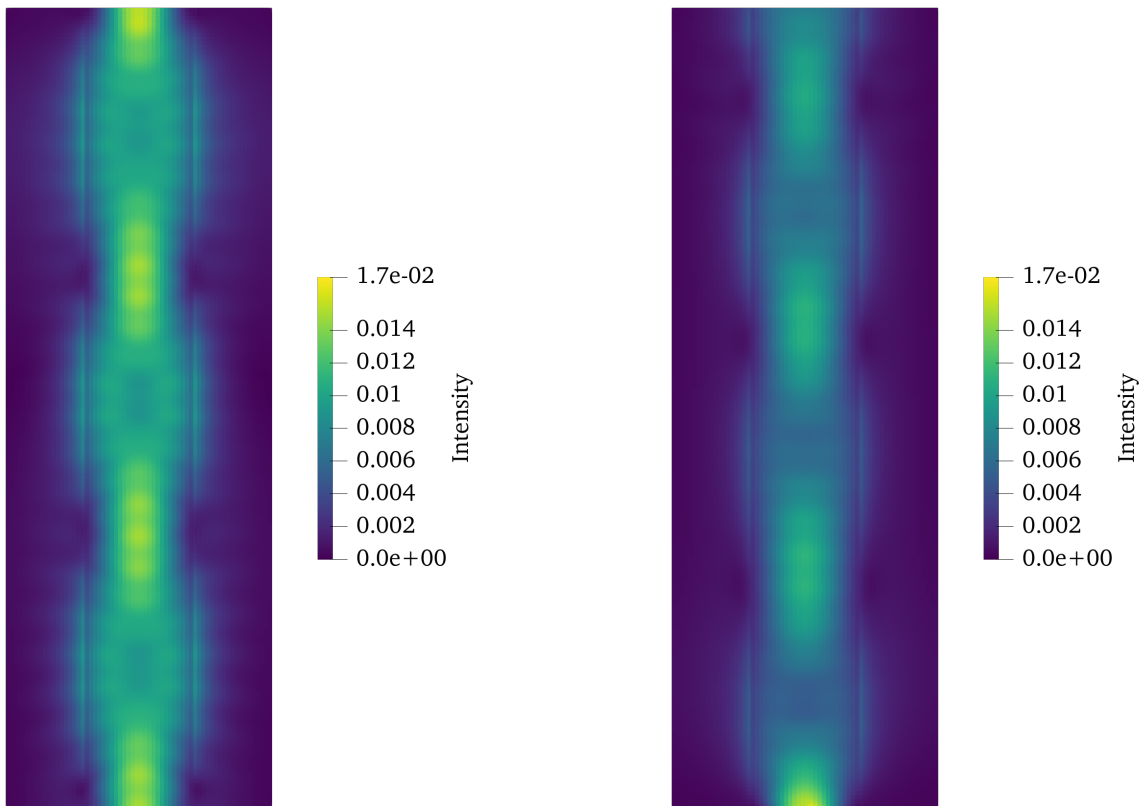


Figure 5.11: **Left:** Intensity plot of the electric field in the two-dimensional waveguide. **Right:** Cross-section of the three-dimensional waveguide at the plane $(0, 2) \times \{1\} \times (0, 6) \mu\text{m}$. Intensity plot of the electric field inside of the three-dimensional waveguide.

| ranks | dofs | Overlap | | | | | |
|-------|--------|------------------|-----------------------------|-------------------|------------------------------|-------------------|------------------------------|
| | | $\delta/H = 5\%$ | $t_{5\%}^{\text{walltime}}$ | $\delta/H = 10\%$ | $t_{10\%}^{\text{walltime}}$ | $\delta/H = 20\%$ | $t_{20\%}^{\text{walltime}}$ |
| 2 | 832 | 12 | 0.08 s | 12 | 0.09 s | 8 | 0.09 s |
| 8 | 3 200 | 37 | 0.14 s | 33 | 0.16 s | 23 | 0.17 s |
| 32 | 12 544 | 100 | 0.37 s | 86 | 0.40 s | 70 | 0.44 s |
| 128 | 49 664 | 405 | 7.73 s | 223 | 4.94 s | 176 | 9.16 s |

Table 5.6: Overview of the wall times and the number of GMRES iterations required to solve the two-dimensional simple waveguide using the ORAS preconditioner in dependence on the number of used ranks, which corresponds to the number of subdomains and the overlap between the subdomains.

| ranks | dofs | Overlap | | | | | |
|-------|-----------|------------------|-----------------------------|-------------------|------------------------------|-------------------|------------------------------|
| | | $\delta/H = 5\%$ | $t_{5\%}^{\text{walltime}}$ | $\delta/H = 10\%$ | $t_{10\%}^{\text{walltime}}$ | $\delta/H = 20\%$ | $t_{20\%}^{\text{walltime}}$ |
| 2 | 81 056 | 12 | 42.6 s | 10 | 43.8 s | 9 | 46.8 s |
| 16 | 618 816 | 94 | 61.6 s | 75 | 66.6 s | 48 | 85.6 s |
| 128 | 4 833 920 | 397 | 356.0 s | 155 | 246.0 s | 129 | 374.0 s |

Table 5.7: Overview of the wall times and the number of GMRES iterations required to solve the three-dimensional simple waveguide using the ORAS preconditioner dependent on the number of used ranks and the overlap between the subdomains.

Configuration, boundary conditions, quantities of interest The waveguide is modeled inside the domain $\Omega = (0, W) \times (0, H) \times (0, L) = (0, 2) \times (0, 2) \times (0, 6) \mu\text{m}$, which includes a cylinder of radius $R = 0.4 \mu\text{m}$ structure at its core. The geometry of the model is shown in Figure 5.10 (right). Moreover, $\Gamma_{\text{inc}} = (0, 2) \times (0, 2) \times \{0\} \mu\text{m}$ is the boundary with the incident boundary condition. All other boundaries, represented by Γ_{∞} , are characterized by absorbing conditions. As mentioned above, we employ homogeneous Robin conditions as absorbing boundary conditions. The incident electric field is modeled by $u_{\text{inc}} = \exp(-100/\mu\text{m}^2(x^2 + y^2)) \vec{e}_x$, where \vec{e}_x is the unit vector in the x -direction.

Physics results The intensity distribution of the electric field forming inside the three-dimensional waveguide is shown in Figure 5.11 (right).

Solver analysis As in the previous example, we study the correlation between the number of subdomains and the number of GMRES iterations. To keep the number of elements per subdomain constant in the three-dimensional setting, the number of subdomains has to be multiplied by a factor of eight for every global refinement. The results are shown in Table 5.7.

5.2.3 Example 3: Y-Beamsplitter

As a last example, we consider a real-world problem, that is, a so-called y-beam splitter, where we have one waveguide as input and two waveguides as output. This example is closely related to the problem discussed in [7].

Configuration, boundary conditions, quantities of interest The y-beam splitter is modeled inside the domain $\Omega = (0.0, 3.2) \times (0.0, 1.2) \times (0.0, 6.4) \mu\text{m}$, where the geometry of the y-beam splitter itself is shown in Figure 5.12 (left). The width and the height of the waveguides the y-beam splitter consists of are $W = 0.8 \mu\text{m}$, $L_{\text{lower}} = 0.8 \mu\text{m}$, $L_{\text{upper}} = 5.6 \mu\text{m}$, and the gap

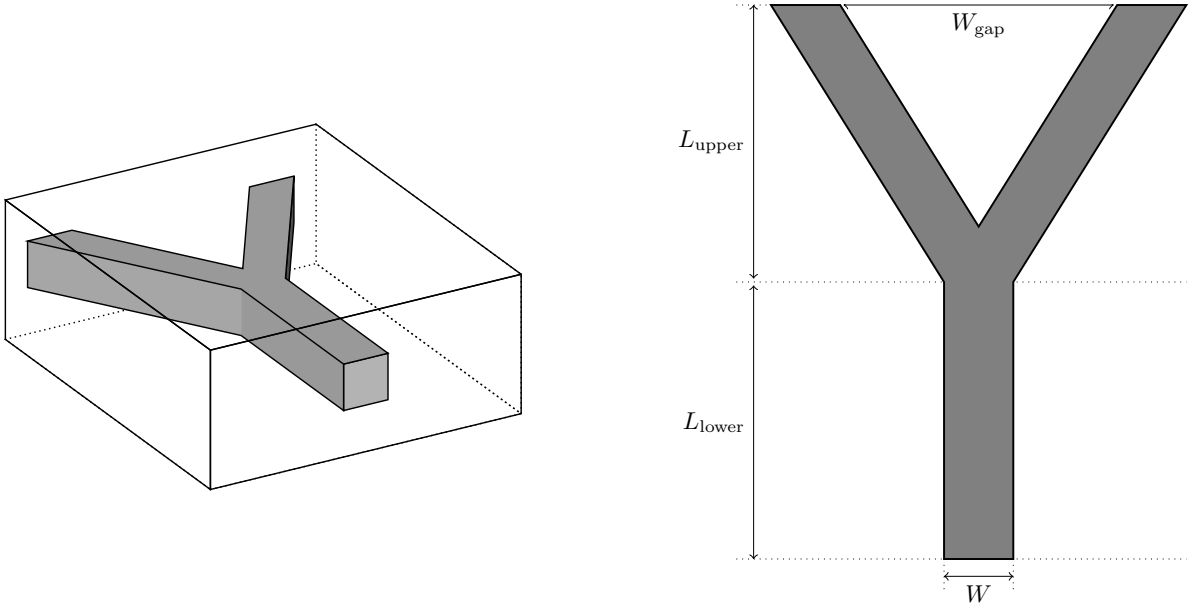


Figure 5.12: **Left:** The orientation of the y-beam splitter inside of the cladding. **Right:** A top-down view of the y-beam splitter, with labels for important geometric characteristics.

between the ends of the outgoing waveguides is $W_{\text{gap}} = 0.4 \mu\text{m}$; see Figure 5.12 (right). The incident electric field is modeled by $u_{\text{inc}} = \exp(-100/\mu\text{m}^2(x^2 + y^2)) \vec{e}_x$, where \vec{e}_x is the unit vector in the x -direction.

Physics results The solution of the y-beam splitter is challenging for two reasons. First, a sufficiently small mesh element size must be chosen based on the y-beam splitter size and the electric field’s wave-like nature. At least four degrees of freedom per wave are required; otherwise, the wave-like nature cannot be resolved. Second, the splitting point introduces a lot of reflection, making the problem harder to solve. We can also observe both of these problems here, as discussed in the solver analysis below. But with a sufficiently large overlap, i.e., $\delta \geq 10\%$, the y-beam splitter can be efficiently solved with the ORAS preconditioner. Our results are displayed graphically in Figure 5.13.

Solver analysis In this example, a convergence analysis is more cumbersome. As discussed above, a sufficiently small step width is required to capture the wave-like nature of the electric field. The two smaller examples, with 112 964, and 856 168 dofs, respectively, are insufficient to resolve the single waves. Therefore, it would be reasonable to start with an even higher initial refinement, requiring additional computational resources, which will not provide more insight into the performance of the deal.II - FROSch interface and these are therefore left for future HPC simulation studies of practical applications within the excellence cluster PhoenixD. The relatively low initial refinement explains why we observe a large jump in the iteration count in the case of an overlap of 5% between 16 and 128 subdomains. For 5% overlap, we only observe poor convergence. Our results are shown in Table 5.8. This highlights that a sufficient overlap must be chosen for more complex problems. Alternatively, more advanced interface conditions can be employed, e.g., high-order approximations as proposed in [28] or PML-based interface conditions [10].

Our findings in Table 5.8 indicate that a 10% overlap is also sufficient for more complex problems. A larger overlap is required to ensure convergence even for even more complex problems, e.g., problems with a high amount of internal reflection.

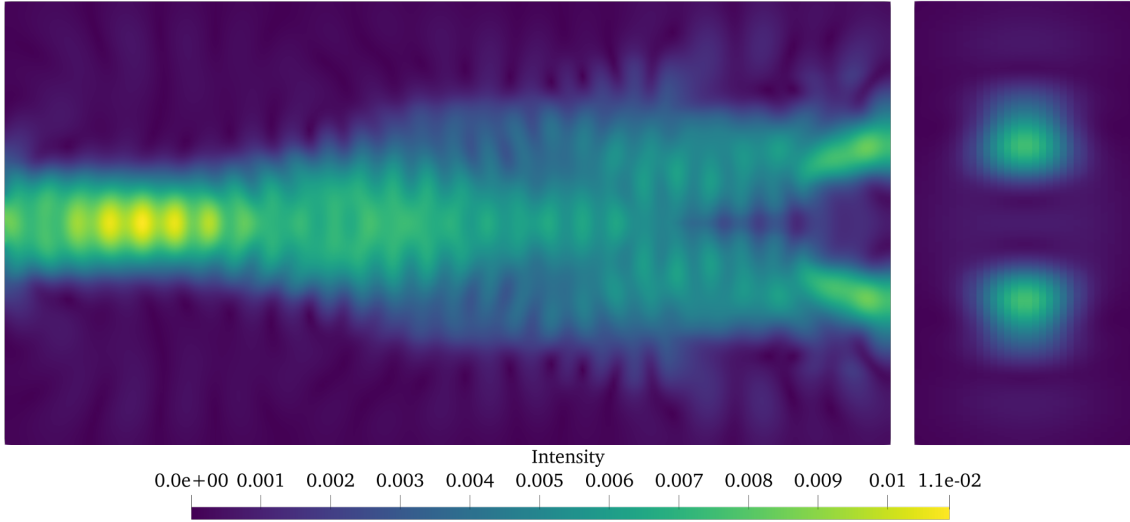


Figure 5.13: **Left:** Cross-section of the y-beam splitter at the plane $(0.0, 3.2) \times \{0.6\} \times (0.0, 6.4) \mu\text{m}$ showing the Intensity distribution of the electric field inside of the y-beam splitter. **Right:** The intensity distribution of the output after splitting one input into two outputs.

| ranks | dofs | Overlap | | | | | |
|-------|-----------|------------------|-----------------------------|-------------------|------------------------------|-------------------|------------------------------|
| | | $\delta/H = 5\%$ | $t_{5\%}^{\text{walltime}}$ | $\delta/H = 10\%$ | $t_{10\%}^{\text{walltime}}$ | $\delta/H = 20\%$ | $t_{20\%}^{\text{walltime}}$ |
| 2 | 112 964 | 17 | 61.4 s | 12 | 63.1 s | 11 | 65.5 s |
| 16 | 856 168 | 178 | 97.9 s | 66 | 98.6 s | 58 | 127.0 s |
| 128 | 6 661 712 | > 1000 | — | 200 | 416.0 s | 171 | 568.0 s |

Table 5.8: Overview of the wall times and the number of GMRES iterations required to solve the three-dimensional y-beam splitter using the ORAS preconditioner dependent on the number of ranks and the overlap between the subdomains.

6 Conclusions

In this work, we considered RAS preconditioners and optimized RAS preconditioners for the iterative GMRES linear solution within linear PDEs and within Newton’s methods for solving nonlinear, coupled PDE systems. Both classical Lagrange-based finite elements and Nédélec finite elements work in our implementation. The main technical work was the design, implementation, and debugging of the optimized Schwarz preconditioners in `FROSch` as well as of the `Tpetra`-based interface between the solver package `FROSch` and the finite element library `deal.II`.

To demonstrate the performance, as model problems, two challenging systems were chosen. First, nonstationary, nonlinear FSI problems were considered. The efficient solution of FSI remains an imminent problem, and open-source implementations in reliable, sustainable software packages remain rare. Due to the nonlinearities, a Newton solver with line search was utilized, while the GMRES solvers with RAS preconditioners were used for the arising linear equation systems. For verification of the correct physics, the typical characteristic quantities of the benchmark problems were considered, and good agreement with the published literature was observed. The analysis of the RAS preconditioners showed good performance in two and three-dimensional numerical examples. Second, indefinite Maxwell’s equations were considered, which remain challenging in their efficient and robust numerical solution. Again, we observed a very good performance of the ORAS preconditioner. The overall conclusion of this work is to have a very easy-to-use software interface while still giving satisfactory solver performances for challenging PDE problems. Thus, we have obtained very promising findings for the novel sustainable interface between `FROSch` and `deal.II` that can be further applied to other linear and nonlinear PDEs and coupled PDE systems.

Acknowledgments

This work is funded by the Deutsche Forschungsgemeinschaft (DFG) under Germany’s Excellence Strategy within the Cluster of Excellence PhoenixD (EXC 2122, Project ID 390833453). Furthermore, we would like to thank Jan Philipp Thiele for many fruitful discussions on the `Tpetra` interface of `deal.II`, and Sven Beuchler for helpful discussions about preconditioners.

References

- [1] P.R. Amestoy, A. Buttari, J.-Y. L’Excellent, and T. Mary. 2019. Performance and Scalability of the Block Low-Rank Multifrontal Factorization on Multicore Architectures. *ACM Trans. Math. Software* 45 (2019), 2:1–2:26. Issue 1.
- [2] D. Arndt, W. Bangerth, M. Bergbauer, M. Feder, M. Fehling, J. Heinz, T. Heister, L. Heltai, M. Kronbichler, M. Maier, P. Munch, J.-P. Pelteret, B. Turcksin, D. Wells, and S. Zampini. 2023. The `deal.II` Library, Version 9.5. *Journal of Numerical Mathematics* 31, 3 (2023), 231–246. <https://doi.org/10.1515/jnma-2023-0089>
- [3] D. Arndt, W. Bangerth, D. Davydov, T. Heister, L. Heltai, M. Kronbichler, M. Maier, J.-P. Pelteret, B. Turcksin, and D. Wells. 2021. The `deal.II` finite element library: Design, features, and insights. *Computers & Mathematics with Applications* 81 (2021), 407–422. <https://doi.org/10.1016/j.camwa.2020.02.022>
- [4] A. T. Barker and X.-C. Cai. 2010. Two-Level Newton and Hybrid Schwarz Preconditioners for Fluid-Structure Interaction. *SIAM Journal on Scientific Computing* 32, 4 (Jan. 2010), 2395–2417. <https://doi.org/10.1137/090779425> Publisher: Society for Industrial and Applied Mathematics.

- [5] E. Bavier, M. Hoemmen, S. Rajamanickam, and H. Thornquist. 2012. Amesos2 and Belos: Direct and iterative solvers for large sparse linear systems. *Scientific Programming* 20, 3 (Jan. 2012), 241–255. <https://doi.org/10.3233/SPR-2012-0352> Publisher: IOS Press.
- [6] Y. Bazilevs, K. Takizawa, and T.E. Tezduyar. 2013. *Computational Fluid-Structure Interaction: Methods and Applications*. Wiley.
- [7] S. Beuchler, S. Kinnewig, and T. Wick. 2022. Parallel Domain Decomposition Solvers for the Time Harmonic Maxwell Equations. In *Domain Decomposition Methods in Science and Engineering XXVI*, Susanne C. Brenner, Eric Chung, Axel Klawonn, Felix Kwok, Jinchao Xu, and Jun Zou (Eds.). Springer International Publishing, Cham, 653–660. https://doi.org/10.1007/978-3-030-95025-5_71
- [8] E. G. Boman, Ü. V. Çatalyürek, C. Chevalier, and K. D. Devine. 2012. The Zoltan and Isorropia parallel toolkits for combinatorial scientific computing: Partitioning, ordering and coloring. *Sci. Program.* 20, 2 (April 2012), 129–150. <https://doi.org/10.1155/2012/713587>
- [9] N. Bootland, S. Borzooei, V. Dolean, and P.-H. Tournier. 2024. Numerical Assessment of PML Transmission Conditions in a Domain Decomposition Method for the Helmholtz Equation. In *Domain Decomposition Methods in Science and Engineering XXVII*, Zdeněk Dostál, Tomáš Kozubek, Axel Klawonn, Ulrich Langer, Luca F. Pavarino, Jakub Šístek, and Olof B. Widlund (Eds.). Springer Nature Switzerland, Cham, 445–453. https://doi.org/10.1007/978-3-031-50769-4_53
- [10] S. Borzooei, V. Dolean, P.-H. Tournier, and C. Migliaccio. 2024. Solution of Time-Harmonic Maxwell’s Equations by a Domain Decomposition Method Based on PML Transmission Conditions. In *Scientific Computing in Electrical Engineering*, Martijn van Beurden, Neil V. Budko, Gabriela Ciuprina, Wil Schilders, Harshit Bansal, and Ruxandra Barbulescu (Eds.). Springer Nature Switzerland, Cham, 45–52. https://doi.org/10.1007/978-3-031-54517-7_5
- [11] H.-J. Bungartz, M. Mehl, and M. Schäfer. 2010. *Fluid-Structure Interaction II: Modelling, Simulation, Optimization*. Springer.
- [12] C. Burstedde, L. C. Wilcox, and O. Ghattas. 2011. p4est: Scalable Algorithms for Parallel Adaptive Mesh Refinement on Forests of Octrees. *SIAM Journal on Scientific Computing* 33, 3 (2011), 1103–1133. <https://doi.org/10.1137/100791634>
- [13] X.-C. Cai and M. Sarkis. 1999. A Restricted Additive Schwarz Preconditioner for General Sparse Linear Systems. *SIAM Journal on Scientific Computing* 21, 2 (Jan. 1999), 792–797. <https://doi.org/10.1137/S106482759732678X> Publisher: Society for Industrial and Applied Mathematics.
- [14] J.-M. Cros. 2003. A preconditioner for the Schur complement domain decomposition method. In *Domain Decomposition Methods in Science and Engineering*, O. Widlund I. Herrera, D. Keyes and R. Yates (Eds.). National Autonomous University of Mexico (UNAM), Mexico City, Mexico, ISBN 970-32-0859-2, 373–380.
- [15] P. Crosetto, S. Deparis, G. Fourestey, and A. Quarteroni. 2011. Parallel algorithms for fluid-structure interaction problems in haemodynamics. *SIAM J. Sci. Comp.* 33, 4 (2011), 1598–1622.
- [16] S. Deparis, D. Forti, G. Grandperrin, and A. Quarteroni. 2016. FaCSI: A block parallel preconditioner for fluid-structure interaction in hemodynamics. *J. Comput. Phys.* 327 (2016), 700–718.

- [17] S. Deparis, D. Forti, A. Heinlein, A. Klawonn, A. Quarteroni, and O. Rheinbach. 2015. A Comparison of Preconditioners for the Steklov–Poincaré Formulation of the Fluid-Structure Coupling in Hemodynamics. *PAMM* 15, 1 (2015), 93–94. Publisher: Wiley Online Library.
- [18] C. R. Dohrmann. 2003. A preconditioner for substructuring based on constrained energy minimization. *SIAM Journal on Scientific Computing* 25, 1 (2003), 246–258. <https://doi.org/10.1137/S1064827502412887>
- [19] C. R. Dohrmann, A. Klawonn, and O. B. Widlund. 2008. Domain decomposition for less regular subdomains: overlapping Schwarz in two dimensions. *SIAM J. Numer. Anal.* 46, 4 (2008), 2153–2168. <https://doi.org/10.1137/070685841>
- [20] C. R. Dohrmann, A. Klawonn, and O. B. Widlund. 2008. A family of energy minimizing coarse spaces for overlapping Schwarz preconditioners. In *Domain decomposition methods in science and engineering XVII*. Lect. Notes Comput. Sci. Eng., Vol. 60. Springer, Berlin, 247–254. https://doi.org/10.1007/978-3-540-75199-1_28
- [21] C. R. Dohrmann and O. B. Widlund. 2017. On the Design of Small Coarse Spaces for Domain Decomposition Algorithms. *SIAM Journal on Scientific Computing* 39, 4 (Jan. 2017), A1466–A1488. <https://doi.org/10.1137/17M1114272> Publisher: Society for Industrial and Applied Mathematics.
- [22] V. Dolean, M. J. Gander, and L. Gerardo-Giorda. 2009. Optimized Schwarz Methods for Maxwell’s Equations. *SIAM Journal on Scientific Computing* 31, 3 (2009), 2193–2213. <https://doi.org/10.1137/080728536>
- [23] V. Dolean, P. Jolivet, and F. Nataf. 2015. *An Introduction to Domain Decomposition Methods: Algorithms, Theory, and Parallel Implementation*. Society for Industrial and Applied Mathematics, Philadelphia, PA. <https://doi.org/10.1137/1.9781611974065>
- [24] J. Donéa, P. Fasoli-Stella, and S. Giuliani. 1977. Lagrangian and Eulerian finite element techniques for transient fluid-structure interaction problems. In *Trans. 4th Int. Conf. on Structural Mechanics in Reactor Technology*. Paper B1/2.
- [25] J. Donea, A. Huerta, J.-Ph. Ponthot, and A. Rodriguez-Ferran. 2004. *Arbitrary Lagrangian-Eulerian methods*. John Wiley and Sons, 1–25.
- [26] T. Dunne. 2006. An Eulerian approach to fluid-structure interaction and goal-oriented mesh adaption. *Int. J. Numer. Methods in Fluids* 51 (2006), 1017–1039.
- [27] E. Efstathiou and M. J. Gander. 2003. Why restricted additive Schwarz converges faster than additive Schwarz. *BIT. Numerical Mathematics* 43, suppl. (2003), 945–959. <https://doi.org/10.1023/B:BITN.0000014563.33622.1d>
- [28] M. El Bouajaji, B. Thierry, X. Antoine, and C. Geuzaine. 2015. A quasi-optimal domain decomposition algorithm for the time-harmonic Maxwell’s equations. *J. Comput. Phys.* 294 (2015), 38–57. <https://doi.org/10.1016/j.jcp.2015.03.041>
- [29] O. G. Ernst and M. J. Gander. 2012. Why it is difficult to solve Helmholtz problems with classical iterative methods. In *Numerical analysis of multiscale problems*. Lect. Notes Comput. Sci. Eng., Vol. 83. Springer, Heidelberg, 325–363. https://doi.org/10.1007/978-3-642-22061-6_10
- [30] C. Farhat, M. Lesoinne, P. LeTallec, K. Pierson, and D. Rixen. 2001. FETI-DP: a dual–primal unified FETI method—part I: A faster alternative to the two-level FETI method. *Internat. J. Numer. Methods Engrg.* 50, 7 (2001), 1523–1544. <https://doi.org/10.1002/nme.76>

- [31] C. Farhat, M. Lesoinne, and K. Pierson. 2000. A scalable dual-primal domain decomposition method. *Numerical Linear Algebra with Applications* 7, 7-8 (2000), 687–714. [https://doi.org/10.1002/1099-1506\(200010/12\)7:7/8<687::AID-NLA219>3.0.CO;2-S](https://doi.org/10.1002/1099-1506(200010/12)7:7/8<687::AID-NLA219>3.0.CO;2-S)
- [32] R. P. Feynman, R. B. Leighton, and M. Sands. 1963. *The Feynman Lectures on Physics. Vol. II. Mainly Electromagnetism and Matter*. California Institute of Technology, Michael A. Gottlieb and Rudolf Pfeiffer.
- [33] L. Formaggia and F. Nobile. 1999. A stability analysis for the Arbitrary Lagrangian Eulerian Formulation with Finite Elements. *East-West Journal of Numerical Mathematics* 7 (1999), 105 – 132.
- [34] D. Forti, A. Quarteroni, and S. Deparis. 2017. A parallel algorithm for the solution of large-scale nonconforming fluid-structure interaction problems in hemodynamics. *J. Comput. Math.* 35, 3 (2017), 363–380.
- [35] G. Galdi and R. Rannacher. 2010. *Fundamental Trends in Fluid-Structure Interaction*. World Scientific. 293 pages.
- [36] M. J. Gander. 2006. Optimized Schwarz Methods. *SIAM J. Numer. Anal.* 44, 2 (2006), 699–731. <https://doi.org/10.1137/S0036142903425409>
- [37] M. J. Gander and H. Zhang. 2016. Optimized Schwarz Methods with Overlap for the Helmholtz Equation. *SIAM Journal on Scientific Computing* 38, 5 (2016), A3195–A3219. <https://doi.org/10.1137/15M1021659>
- [38] M. W. Gee, U. Küttler, and W. A. Wall. 2011. Truly monolithic algebraic multigrid for fluid–structure interaction. *Int. J. Numer. Meth. Engrg.* 85, 8 (2011), 987–1016.
- [39] C. Goll, T. Wick, and W. Wollner. 2017. DOpElib: Differential Equations and Optimization Environment; A Goal Oriented Software Library for Solving PDEs and Optimization Problems with PDEs. *Archive of Numerical Software* 5, 2 (2017), 1–14. <https://doi.org/10.11588/ans.2017.2.11815>
- [40] A. V. Grayver and T. V. Kolev. 2015. Large-Scale 3D Geoelectromagnetic Modeling Using Parallel Adaptive High-Order Finite Element Method. *Geophysics* 80, 6 (2015), E277–E291. <https://doi.org/10.1190/geo2015-0013.1>
- [41] M. Heil. 2004. An efficient solver for the fully coupled solution of large-displacement fluid-structure interaction problems. *Comput. Methods Appl. Mech. Engrg.* 193 (2004), 1–23.
- [42] A. Heinlein. 2016. *Parallel overlapping Schwarz preconditioners and multiscale discretizations with applications to fluid-structure interaction and highly heterogeneous problems*. PhD Thesis. Universität zu Köln.
- [43] A. Heinlein, C. Hochmuth, and A. Klawonn. 2019. Monolithic overlapping Schwarz domain decomposition methods with GDSW coarse spaces for incompressible fluid flow problems. *SIAM Journal on Scientific Computing* 41, 4 (2019), C291–C316. <https://doi.org/10.1137/18M1184047>
- [44] A. Heinlein, C. Hochmuth, and A. Klawonn. 2021. Fully algebraic two-level overlapping Schwarz preconditioners for elasticity problems. In *Numerical mathematics and advanced applications—ENUMATH 2019 (Lect. Notes Comput. Sci. Eng., Vol. 139)*. Springer, Cham, 531–539. https://doi.org/10.1007/978-3-030-55874-1_52

- [45] A. Heinlein, A. Klawonn, J. Knepper, and O. Rheinbach. 2019. Adaptive GDSW coarse spaces for overlapping Schwarz methods in three dimensions. *SIAM Journal on Scientific Computing* 41, 5 (2019), A3045–A3072. <https://doi.org/10.1137/18M1220613>
- [46] A. Heinlein, A. Klawonn, S. Rajamanickam, and O. Rheinbach. 2020. FROSch: a fast and robust overlapping Schwarz domain decomposition preconditioner based on Xpetra in Trilinos. In *Domain decomposition methods in science and engineering XXV (Lect. Notes Comput. Sci. Eng., Vol. 138)*. Springer, Cham, 176–184. https://doi.org/10.1007/978-3-030-56750-7_19
- [47] A. Heinlein, A. Klawonn, and O. Rheinbach. 2016. A parallel implementation of a two-level overlapping Schwarz method with energy-minimizing coarse space based on Trilinos. *SIAM Journal on Scientific Computing* 38, 6 (2016), C713–C747. <https://doi.org/10.1137/16M1062843>
- [48] A. Heinlein, A. Klawonn, and O. Rheinbach. 2016. Parallel two-level overlapping Schwarz methods in fluid-structure interaction. In *Numerical mathematics and advanced applications—ENUMATH 2015 (Lect. Notes Comput. Sci. Eng., Vol. 112)*. Springer, [Cham], 521–530. https://doi.org/10.1007/978-3-319-39929-4_5
- [49] A. Heinlein, A. Klawonn, O. Rheinbach, and O. B. Widlund. 2018. Improving the parallel performance of overlapping Schwarz methods by using a smaller energy minimizing coarse space. In *Domain decomposition methods in science and engineering XXIV (Lect. Notes Comput. Sci. Eng., Vol. 125)*. Springer, Cham, 383–392. https://doi.org/10.1007/978-3-319-93873-8_3
- [50] A. Heinlein, M. Perego, and S. Rajamanickam. 2022. FROSch Preconditioners for Land Ice Simulations of Greenland and Antarctica. *SIAM Journal on Scientific Computing* 44, 2 (April 2022), B339–B367. <https://doi.org/10.1137/21M1395260> Publisher: Society for Industrial and Applied Mathematics.
- [51] A. Heinlein, O. Rheinbach, and F. Röver. 2022. Parallel Scalability of Three-Level FROSch Preconditioners to 220000 Cores using the Theta Supercomputer. *SIAM Journal on Scientific Computing* (Aug. 2022), S173–S198. <https://doi.org/10.1137/21M1431205> Publisher: Society for Industrial and Applied Mathematics.
- [52] A. Heinlein, O. Rheinbach, and F. Röver. 2023. A Multilevel Extension of the GDSW Overlapping Schwarz Preconditioner in Two Dimensions. *Computational Methods in Applied Mathematics* 23, 4 (Oct. 2023), 953–968. <https://doi.org/10.1515/cmam-2022-0168> Publisher: De Gruyter.
- [53] T. Heister and T. Wick. 2020. pfm-cracks: A parallel-adaptive framework for phase-field fracture propagation. *Software Impacts* 6 (2020), 100045. <https://doi.org/10.1016/j.simpa.2020.100045>
- [54] M. A. Heroux, R. A. Bartlett, V. E. Howle, R. J. Hoekstra, J. J. Hu, T. G. Kolda, R. B. Lehoucq, K. R. Long, R. P. Pawlowski, E. T. Phipps, A. G. Salinger, H. K. Thornquist, R. S. Tuminaro, J. M. Willenbring, A. Williams, and K. S. Stanley. 2005. An overview of the Trilinos Project. *Association for Computing Machinery. Transactions on Mathematical Software* 31, 3 (2005), 397–423. <https://doi.org/10.1145/1089014.1089021>
- [55] J. G. Heywood, R. Rannacher, and S. Turek. 1996. Artificial boundaries and flux and pressure conditions for the incompressible Navier-Stokes Equations. *International Journal of Numerical Methods in Fluids* 22 (1996), 325–352.

- [56] J. Hron and S. Turek. 2006. *Proposal for numerical benchmarking of fluid-structure interaction between an elastic object and laminar incompressible flow*. Vol. 53. Springer-Verlag, 146–170.
- [57] T.J.R. Hughes, W.K. Liu, and T Zimmermann. 1981. Lagrangian-Eulerian finite element formulation for incompressible viscous flows. *Comput. Methods Appl. Mech. Engrg.* 29 (1981), 329–349.
- [58] N. M. M. Huynh, L. F. Pavarino, and S. Scacchi. 2024. GDSW preconditioners for composite Discontinuous Galerkin discretizations of multicompartment reaction-diffusion problems. <https://doi.org/10.48550/arXiv.2405.17601> arXiv:2405.17601 [cs, math].
- [59] D. Jodlbauer, U. Langer, and T. Wick. 2019. Parallel block-preconditioned monolithic solvers for fluid-structure interaction problems. *Int. J. Num. Meth. Eng.* 117, 6 (2019), 623–643.
- [60] G. Karypis and V. Kumar. 1998. A Fast and High Quality Multilevel Scheme for Partitioning Irregular Graphs. *SIAM Journal on Scientific Computing* 20, 1 (Jan. 1998), 359–392. <https://doi.org/10.1137/S1064827595287997> Publisher: Society for Industrial and Applied Mathematics.
- [61] S. Kinnewig, T. Wick, and S. Beuchler. 2023. Algorithmic realization of the solution to the sign conflict problem for hanging nodes on hp-hexahedral Nédélec elements. (2023). arXiv:2306.01416 [math.NA]
- [62] P.-L. Lions. 1988. On the Schwarz alternating method. I. In *First International Symposium on Domain Decomposition Methods for Partial Differential Equations (Paris, 1987)*. SIAM, Philadelphia, PA, 1–42. <https://mathscinet.ams.org/mathscinet-getitem?mr=972510>
- [63] H. Mahmudlu, R. Johanning, A. Van Rees, A. Khodadad Kashi, J. P. Epping, R. Haldar, K.-J. Boller, and M. Kues. 2023. Fully On-Chip Photonic Turnkey Quantum Source for Entangled Qubit/Qudit State Generation. *Nature Photonics* (2023). <https://doi.org/10.1038/s41566-023-01193-1>
- [64] O. Melchert, S. Kinnewig, F. Dencker, D. Perevoznik, S. Willms, I. V. Babushkin, M. C. Wurz, M. Kues, S. Beuchler, T. Wick, U. Morgner, and A. Demircan. 2023. Soliton Compression and Supercontinuum Spectra in Nonlinear Diamond Photonics. *Diamond and Related Materials* 136 (2023), 109939. <https://doi.org/10.1016/j.diamond.2023.109939>
- [65] P. Monk. 2003. *Finite Element Methods for Maxwell’s Equations*. Clarendon Press ; Oxford University Press, Oxford : New York.
- [66] R. A. Nicolaides. 1987. Deflation of conjugate gradients with applications to boundary value problems. *SIAM J. Numer. Anal.* 24, 2 (1987), 355–365. <https://doi.org/10.1137/0724027>
- [67] A. Quarteroni and A. Valli. 1999. *Domain Decomposition Methods for Partial Differential Equations*. Oxford University Press, Oxford, New York.
- [68] S. Rajamanickam, S. Acer, L. Berger-Vergiat, V. Dang, N. Ellingwood, E. Harvey, B. Kelley, C. R. Trott, J. Wilke, and I. Yamazaki. 2021. Kokkos Kernels: Performance Portable Sparse/Dense Linear Algebra and Graph Kernels. <https://doi.org/10.48550/arXiv.2103.11991> arXiv:2103.11991 [cs].
- [69] T. Richter. 2017. *Fluid-structure interactions: models, analysis, and finite elements*. Springer.

- [70] Y. Saad and M. H. Schultz. 1986. GMRES: a generalized minimal residual algorithm for solving nonsymmetric linear systems. *Society for Industrial and Applied Mathematics. Journal on Scientific and Statistical Computing* 7, 3 (1986), 856–869. <https://doi.org/10.1137/0907058>
- [71] B. F. Smith, P. E. Bjørstad, and W. D. Gropp. 1996. *Domain decomposition*. Cambridge University Press, Cambridge. <https://mathscinet.ams.org/mathscinet-getitem?mr=1410757>
- [72] A. St-Cyr, M. J. Gander, and S. J. Thomas. 2007. Optimized multiplicative, additive, and restricted additive Schwarz preconditioning. *SIAM Journal on Scientific Computing* 29, 6 (2007), 2402–2425. <https://doi.org/10.1137/060652610>
- [73] A. Toselli and O. Widlund. 2005. *Domain decomposition methods—algorithms and theory*. Springer Series in Computational Mathematics, Vol. 34. Springer-Verlag, Berlin. <https://doi.org/10.1007/b137868>
- [74] C. R. Trott, D. Lebrun-Grandié, D. Arndt, J. Ciesko, V. Dang, N. Ellingwood, R. Gayatri, E. Harvey, D. S. Hollman, D. Ibanez, N. Liber, J. Madsen, J. Miles, D. Poliakoff, A. Powell, S. Rajamanickam, M. Simberg, D. Sunderland, B. Turcksin, and J. Wilke. 2022. Kokkos 3: Programming Model Extensions for the Exascale Era. *IEEE Transactions on Parallel and Distributed Systems* 33, 4 (2022), 805–817. <https://doi.org/10.1109/TPDS.2021.3097283>
- [75] M. F. Wheeler, T. Wick, and S. Lee. 2020. IPACS: Integrated Phase-Field Advanced Crack Propagation Simulator. An adaptive, parallel, physics-based-discretization phase-field framework for fracture propagation in porous media. *Computer Methods in Applied Mechanics and Engineering* 367 (2020), 113124. <https://doi.org/10.1016/j.cma.2020.113124>
- [76] T. Wick. 2011. Fluid-Structure Interactions using Different Mesh Motion Techniques. *Comput. & Structures* 89, 13-14 (2011), 1456–1467.
- [77] T. Wick. 2013. Solving Monolithic Fluid-Structure Interaction Problems in Arbitrary Lagrangian Eulerian Coordinates with the deal.II Library. *Archive of Numerical Software* 1 (2013), 1–19. <https://doi.org/10.11588/ans.2013.1.10305>
- [78] T. Wick and W. Wollner. 2021. Optimization with nonstationary, nonlinear monolithic fluid-structure interaction. *Internat. J. Numer. Methods Engrg.* 122, 19 (2021), 5430–5449. <https://doi.org/10.1002/nme.6372>
- [79] Y. Wu and X.-C. Cai. 2011. A parallel two-level method for simulating blood flows in branching arteries with the resistive boundary condition. *Computers & Fluids* 45, 1 (June 2011), 92–102. <https://doi.org/10.1016/j.compfluid.2010.11.015>
- [80] I. Yamazaki, A. Heinlein, and S. Rajamanickam. 2023. An Experimental Study of Two-level Schwarz Domain-Decomposition Preconditioners on GPUs. IEEE Computer Society, 680–689. <https://doi.org/10.1109/IPDPS54959.2023.00073>
- [81] M. Zolgharni, P. D. Ledger, and H. J. Griffiths. 2009. Forward Modelling of Magnetic Induction Tomography: A Sensitivity Study for Detecting Haemorrhagic Cerebral Stroke. *Medical & Biological Engineering & Computing* 47, 12 (2009), 1301–1313. <https://doi.org/10.1007/s11517-009-0541-1>